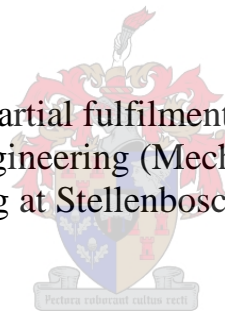


# **SOLAR AIR RECEIVER USING A NON-UNIFORM POROUS MEDIUM**

Philippus Carel van der Merwe

Assignment presented in partial fulfilment of the requirements for the  
degree of Master in Engineering (Mechanical) in the Faculty of  
Engineering at Stellenbosch University



Supervisor: Dr J.E. Hoffmann

March 2016

## DECLARATION

By submitting this assignment electronically, I declare that the entirety of the work contained therein is my own, original work, that I am the sole author thereof (save to the extent explicitly otherwise stated), that reproduction and publication thereof by Stellenbosch University will not infringe any third party rights and that I have not previously in its entirety or in part submitted it for obtaining any qualification.

March 2016

## **ABSTRACT**

A receiver concept for a CSP plant employing a Brayton cycle solar thermal power plant was designed and tested experimentally. The receiver aims to mimic the greenhouse effect and comprises of an annular configuration, with a transparent outer tube and an opaque inner tube. A porous medium in the annular space serves to trap radiation and transfers heat to air flowing through it. The receiver concept may be integrated in any CSP plant exploiting the Brayton Cycle, such as the SUNSPOT system. The receiver will be situated between the compressor and combustor with the aim being to increase the air temperature before it runs through the combustion chamber.

A linear mirror system was developed to concentrate the solar radiation in the receiver tube, while air was used as the heat transfer fluid. The temperature of the air was measured at the outlet of the tube in order to determine the efficiency of the receiver tube.

The projects aims towards determining the radiation properties of the porous medium by means of three different ways. The first modelled developed, was that of an analytical Matlab model and the second being a simulated CFD model. These results were compared to the experimental tested results.

The study concluded that the receiver achieved an efficiency of 41 % without being optimized, while reaching an average temperature increase in the system of up to 40 °C. The radiation properties of the porous medium can, however, not be determined by taking temperature measurements. A separate test result will have to be constructed to determine these properties. The concept proves to be very promising although it only achieved an efficiency of 41 %. The large heat transfer area between the air and the porous medium proves to be a major advantage.

## OPSOMMING

'n Sonstraal ontvanger sisteem is ontwerp om die straling vanaf die son te reflekteer op 'n lineêre lyn waar die ontvanger geplaas is. Hierdie ontvanger word gesien as 'n moontlike konsep om lug te verhit tydens die Brayton siklus in gekonsentreerde son-energie kragstasies. Die ontvanger bestaan uit 'n deurskynende glas, met 'n koper pyp in die middel en 'n annulus wat gevul is met poreuse materiaal. Die konsep is gebaseer op die kweekhuis effek, waar die energie binne 'n deurskynende ruimte geabsorbeer word. Hierdie konsep is ideaal vir die SUNPOT stelsel aangesien dit lug gedrewe is en ook van die Brayton siklus gebruik sal maak. Hierdie stelsel sal tussen die turbine en ontbrandingskamer geplaas word om te temperatuur van die lug te verhoog voor dit deur die turbines gaan.

Die sonstraal ontvanger sisteem het bestaan uit agt lineêre spieëls wat die lig konsentreer op 'n lineêre lyn, 2 m bo die grond oppervlak. Die uitlaat temperatuur was gemeet by verskillende om die totale effektiwiteit van die stelsel te bepaal.

Een van die doelwitte van die projek is ook om die stralings eienskappe van die poreuse materiaal te toets. Hierdie doelwit was op drie verskillende metodes getoets. Eerstens was die ontvanger deur verskillende eksperimentele toetse geplaas. Hierdie eksperimentele toetsdata was dan vergelyk met twee verskillende modelle: 'n analitiese Matlab model en 'n simulatie model wat met behulp van ANSYS geskep is. Die verskillende toetse was met mekaar vergelyk om die moontlike stralings vermoë te bepaal van die poreuse materiaal.

Die studie het bevind dat die ontvanger buis 'n effektiwiteit van 41 % het, sonder om optimalisering toe te pas op die stelsel. 'n Gemiddelde temperatuur verskil van 40 °C was ook bereik by die uitlaat van die stelsel. Daar is egter gevind dat die straling eienskappe van die materiaal nie deur hierdie toets bepaal kan word nie en dat 'n aparte opstelling gedoen moet word. Hierdie konsep is baie belowend en die groot hitte oordrag area tussen die poreuse medium en die lug is van groot voordeel wanneer na alternatiewe konsepte gekyk word.

## **ACKNOWLEDGEMENTS**

The author would like to acknowledge the following people for their contributions toward completing this project. Without their help, it would not have been possible.

Firstly I would like to thank Dr J.E. Hoffmann for all his motivation, support and guidance throughout the project. The author was grateful for a supervisor that made room for the development of the authors' ideas.

Secondly I would like to thank my parents for their continuous support throughout my career. Without their guidance and financial support, none of this would have been possible.

I would also like to thank Ms NF Laurie with the language editing of the report and relentless patience. Thanks to Ms L Kleingbiel for all her guidance, motivation and help with regards to finding funding for the project.

Just a last thank to the M&M staff for the construction of the collector and the STERG team for always being available to help. Being in such an environment is one huge privilege. Thanks to the National Research Foundation (NRF) for funding of this research project.

**TABLE OF CONTENT**

Abstract .....	i
Opsomming .....	ii
Acknowledgements.....	iii
List of Figures .....	vii
List of Tables .....	ix
Nomenclature .....	x
CHAPTER 1. Introduction.....	1
1.1 Different CSP types .....	2
1.2 History of central receiver towers .....	3
1.3 Concentrated solar power in South African context.....	3
1.4 SUNSPOT .....	5
1.5 Current pilot plants using air as working fluid .....	6
1.6 Overview of the designed annular solar air receiver .....	7
1.7 Research objectives and scope .....	8
CHAPTER 2. Literature study .....	9
2.1 Different receiver types available.....	9
2.1.1 Gas receivers .....	9
2.1.2 Liquid receivers.....	10
2.1.3 Solid particle receivers.....	11
2.2 Importance of low pressure losses.....	12
2.3 Radiation properties of participating medium.....	13
2.3.1 Radiative energy losses .....	13
2.3.2 Formulation of radiative transfer equation.....	15
2.4 Porous medium studies.....	16
2.5 Heat transfer analyses.....	17
2.5.1 Air flow analyses in the receiver.....	18

2.5.2	Convection heat transfer to the air .....	19
2.5.3	Conduction in the copper pipe .....	20
2.5.4	Convection and radiation losses from quartz tube to environment .....	20
CHAPTER 3. Design, setup and construction .....		22
3.1	Support and collector structure.....	22
3.2	Tracking.....	25
3.3	Receiver design.....	27
3.4	Final experimental setup.....	28
3.5	The method.....	29
3.5.1	Research designs .....	29
3.5.2	The methodology .....	30
3.5.3	Data .....	32
3.5.4	Analyses .....	33
3.5.5	Conclusion .....	33
CHAPTER 4. Simulation of receiver.....		34
4.1	Assumptions in the numerical Matlab model .....	34
4.2	Energy equation background.....	35
4.3	Numerical Matlab model.....	36
4.3.1	General case .....	38
4.3.2	Boundary conditions .....	39
4.3.3	Formulation of critical constants and variables .....	39
4.4	CFD analyses of receiver.....	40
4.4.1	Model design.....	40
4.4.2	Model setup.....	41
4.4.3	Material specification.....	42
4.4.4	Cell zone conditions.....	42

4.4.5	Boundary conditions .....	43
4.4.6	Data to be collected.....	44
4.5	CFD description of the two-dimensional radiation model .....	44
CHAPTER 5.	Results and analyses .....	45
5.1	Experimental results .....	45
5.2	Numerical Matlab model results.....	48
5.3	Simulation results .....	49
5.4	Combined results and analyses.....	52
5.5	Overall efficiency of receiver .....	54
5.6	Pressure losses in the tube receiver .....	55
5.7	Verification of models .....	55
CHAPTER 6.	Conclusions.....	58
REFERENCES	.....	60
APPENDIX A.	Catalogues and data sheets .....	A-1
APPENDIX B.	MATLAB codes .....	B-1
B.1	The two-dimensional radiation model.....	B-1
B.2	Deflection analyses of structure .....	B-5
APPENDIX C.	Calibration of Instruments .....	C-1
C.1	Calibration of the flow meter and pressure regulator .....	C-1
C.2	Calibration of flux sensor .....	C-4
C.3	Thermocouple calibration.....	C-5
APPENDIX D.	Expenses of project.....	D-1
APPENDIX E.	Dimensioned drawing .....	E-1

**LIST OF FIGURES**

Figure 1: Expected electricity demand vs actual in RSA .....	1
Figure 2: DNI map of South Africa .....	4
Figure 3: The SUNSPOT cycle .....	6
Figure 4: The Jülich solar tower .....	7
Figure 5: The REFOS receiver .....	9
Figure 6: Example of tubular receiver .....	10
Figure 7: The Brayton cycle .....	12
Figure 8: Attenuation of the radiation.....	14
Figure 9: Radiation propagating through a volume element .....	16
Figure 10: Heat transfer diagram of receiver.....	17
Figure 11: Absorption, reflection and transmission by porous medium.....	21
Figure 12: The support structure with receiver.....	22
Figure 13: Structural analyses of the beam.....	23
Figure 14: Sun position angles.....	24
Figure 15: DNI distribution for the 30 <sup>th</sup> of March 2015 .....	24
Figure 16: Multi axis and single axis tracking.....	25
Figure 17: Double axis tracking mechanism .....	26
Figure 18: Tracking sensor .....	27
Figure 19: Vertical cross section of receiver .....	27
Figure 20: Complete receiver design setup.....	28
Figure 21: Experimental setup.....	29
Figure 22: Placement of the thermocouples .....	30
Figure 23: Two different axis used for setup.....	33
Figure 24: Cylindrical coordinate system that will be used.....	34
Figure 25: Cylindrical volume element .....	35
Figure 26: Section of control volume .....	37

Figure 27: Single control volume element.....	37
Figure 28: Node numbering format .....	38
Figure 29: Mesh profile of the receiver .....	40
Figure 30: Edge sizing and face sizing .....	41
Figure 31: Radiation model setup .....	44
Figure 32: Thermal imaging of the receiver .....	45
Figure 33: Measure temperature in test 1 .....	46
Figure 34: Measure temperature in test 2 .....	46
Figure 35: Temperature distribution for different tests .....	47
Figure 36: Temperature profile for different sections .....	47
Figure 37: Evaluating different absorption coefficients .....	48
Figure 38: Radiation flux distribution .....	49
Figure 39: Simulated radiation profile.....	49
Figure 40: Temperature distribution at outlet.....	50
Figure 41: Temperature profile at the outlet.....	51
Figure 42: Temperature profile halfway through the tube.....	51
Figure 43: Streamline temperature of the air .....	52
Figure 44: CFD model compared with experimental data.....	53
Figure 45: Linearized comparison of temperature profiles .....	54
Figure 46: Pressure losses with and without porous medium.....	55
Figure 47: Grid independence test of numerical model.....	56
Figure 48: Verification of different mesh types in simulated model.....	57
Figure 49: Experimental setup.....	C-2
Figure 50: Calibration of the flow meter .....	C-3
Figure 51: Calibration of the pressure regulator .....	C-3
Figure 52: Calibration of the flux at outer surface.....	C-4
Figure 53: Calibration graph of some thermocouples .....	C-5

**LIST OF TABLES**

Table 1: Update on the current CSP projects in RSA.....	5
Table 2: Summary of receivers .....	11
Table 3: Mesh structures of the simulated model .....	56
Table 4: Properties of the glass tube .....	A-1
Table 5: Detail of equipment used.....	A-2
Table 6: Dimensions of bell mouth and orifice plate.....	C-1
Table 7: Temperature difference of all the thermocouples.....	C-6
Table 8: The cost for each activity.....	D-1
Table 9: Expenses for construction of rig.....	D-1
Table 10: Expense of equipment used (depreciation).....	D-2
Table 11: Total project cost .....	D-2

## NOMENCLATURE

### Latin Symbols

<b>Symbol</b>	<b>Description</b>
$A$	Area
$c_p$	Specific heat at constant pressure
$D$	Large diameter
$d$	Small diameter
$h$	Convective heat transfer coefficient
$I$	Radiation intensity
$I_\lambda$	Spectral radiation intensity
$k$	Thermal conductivity / Heat capacity ratio
$l_m$	Penetration length
$Nu$	Nusselt number
$P$	Pressure
$Pr$	Prandtl number
$q$	Energy per unit area
$Re$	Reynolds number
$r_p$	Pressure ratio
$T$	Temperature
$U$	Internal energy
$V$	Flow speed
$W$	Work done
$\dot{V}$	Volumetric flow rate
$\dot{Q}$	Energy rate
$\dot{m}$	Mass flow rate

## Greek Letters

<b>Symbol</b>	<b>Description</b>
$\beta$	Attenuation factor
$\delta$	Deflection
$\varepsilon$	Emissivity / porosity
$\eta_{th}$	Thermal efficiency
$\theta, \Omega$	Angle
$\theta_a$	Solar azimuth angle
$\theta_{el}$	Solar elevation angle
$\kappa$	Absorptivity term
$\lambda$	Wavelength
$\rho$	Density
$\sigma$	Stefan Boltzmann constant
$\sigma_s$	Scattering term
$\tau_{opt}$	Optical thickness
$\Phi$	Phase function
$\varphi$	Deflection angle

## CHAPTER 1. INTRODUCTION

In 2010 South Africa took a step towards committing to the United Nations Framework Convention on Climate Change (UNFCCC). This commitment required the nation to decrease its greenhouse emissions by 34 % by 2020 (Inglesi-Lotz & Blignaut, 2011). More than 60 % of the emission gasses originate from electricity generation, which is predominant from coal-fired power plants. Diversification of South Africa's power supply is thus essential in order to reduce the nation's gas emissions.

To achieve these emission reduction commitments, it is important to understand the underlying problem regarding the increase in power consumption by the country. According to studies conducted by Andrade Silva *et al.* (2009) and Weber (2009), the three main factors which lead to an increase in energy consumption are: production changes, structural change in the economy and energy efficiency improvements.

The expected electricity demand in South Africa will increase significantly in the next five years, as can be seen in Figure 1. The CSIR Green Shoots forecast assume an average Gross Domestic Product (GDP) 5.4 % annually increase until 2013 and an yearly electricity demand increase of 2.7 % (Department of Energy, 2013), which form the base case for all forecasts. This shows that the national grid must not only supply the demand, but must also increase its capacity to accommodate growth in a country.

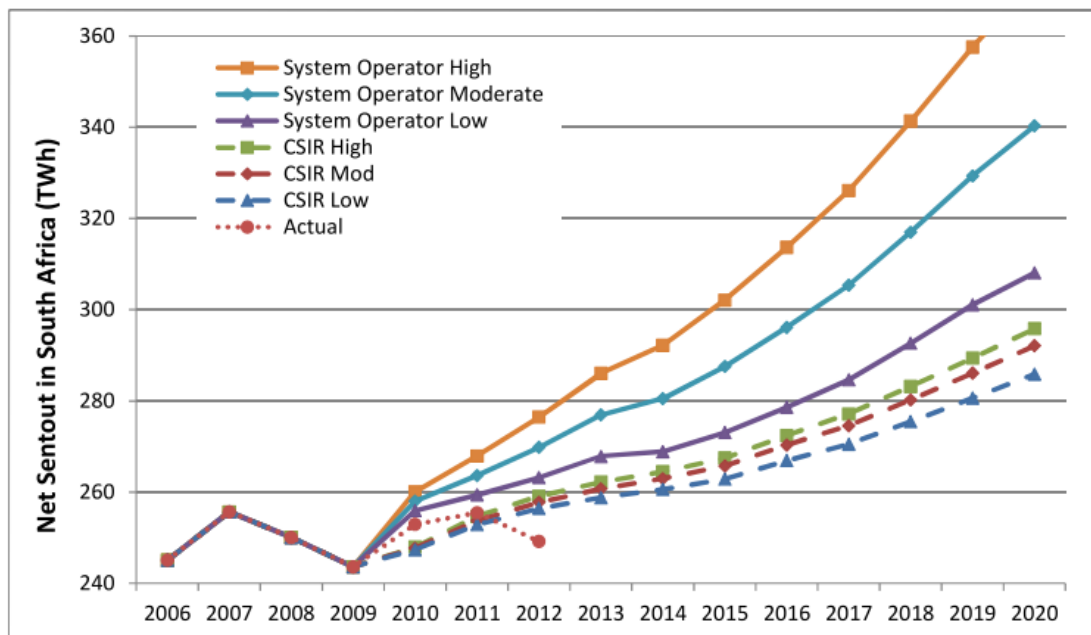


**Figure 1: Expected electricity demand vs actual in RSA**

Source: (Department of Energy, 2013)

Combining the need for an improved GDP, while making a commitment to the UNFCCC to decrease the emission gasses, therefore opens the door for renewable energy projects in South Africa. Furthermore, having one of the best solar sources world-wide, makes South Africa exceptional attractive for the development of solar systems. The different solar technologies will be discussed next with specific focus placed on solar towers and their implications.

### **1.1 Different CSP types**

Concentrated solar power (CSP) uses lenses or mirrors to concentrate solar radiation on a central focal point or focal line. These systems have either single axis or multiple axis tracking installed in order to track the sun. The solar thermal heat is then used as a heat source to power a turbine or to be used in industrial processes for heating or cooling. Concentrated photovoltaic, parabolic troughs, linear Fresnel reflectors, solar power towers and Stirling dishes are the most common technologies available nowadays. Each of these technologies will be discussed as well as the benefits and concerns involved.

The Concentrated Photovoltaic panels use an array of small mirrors on the panel to focus the incoming radiation on multiple small silicon cells. These panels are more or less twice as effective as the traditional photovoltaic panels. Besides the fact that it is more efficient, concentrated photovoltaic panels use less silicon, which is considered as short in supply. The problem, however, is that these panels are very sensitive to cloud cover and can only be used in areas where there is not much cloud cover. These panels are also very sensitive and therefore highly accurate tracking systems must be installed, which make them relative expensive compared to standard panels.

The most mature technology of them all is that of parabolic troughs, since the first reliable operating plant was established in 1970. Parabolic troughs consist of parabolic shaped mirrors that focus the radiation on a centreline where the receivers containing oil or molten salt are connected in series and parallel with each other. The working fluid is transferred to a central point where the thermal energy is converted to electricity by means of turbines. The excess energy can be stored for future use, which makes parabolic trough systems one of the most popular renewable electricity generation technologies.

Linear Fresnel reflectors work on the same principal as the parabolic through principle, but instead of using parabolic shaped mirrors, the Fresnel system uses flat mirrors. This leads to cheaper manufacturing costs and also allows for a greater density of reflectors in an array, achieving a greater concentration ratio.

Solar Towers use heliostats, which are flat square shaped mirrors that track the sun to concentrate the irradiation on a central, elevated point from the ground. Large pumping systems are used to transport the working fluid to the top of the tower, where the solar energy is transferred to the working fluid. This allows for the achievement of higher fluid temperatures, but in turn leads to engineering difficulty with high material temperatures in the receiver (Tian & Zhao, 2013). Solar tower technologies are the fastest developing technology of them all, but also holds the highest risks since the technology is the most immature of them all (Behar, Khellaf & Mohammadi, 2013; Kost, 2013), which leads to difficulties with regards to the funding of these projects.

The last technology that will be discussed is that of Stirling dishes. These systems use large round paraboloid mirrors to focus the irradiation on a centre point where a Stirling engine is placed. The biggest advantage of these systems is the small size scalability since a standalone system can generate as little as 25 kW and still be feasible. These individual systems can be linked together to form a large plant. However, the biggest downside of these systems, is the fact that there is no thermal storage available, which place them in the same market as photovoltaic systems. With photovoltaic being very popular, cheap and matured, there is currently no high demand for Stirling dishes in the market.

## 1.2 History of central receiver towers

The concentrated energy concept is not a new invention at all, the magnifying glass was already developed in the 7<sup>th</sup> Century BC (Hongwei Zhu, Wei, Wang, Wu, Al-Hasan, *et al.*, 2011). These magnifying glasses were then used to light fires, not for the optical functionality like today. However, the first solar tower was only developed in the early 1980's, called Solar One (Hongwei Zhu *et al.*, 2011).

Solar One was a solar thermal project developed by the Department of Energy (DOE), California Energy Commission, Los Angeles Department of Water and Power as well as California Edison. The system used water as a working fluid, which was heated at the top of the tower and transferred to the ground where the boilers were situated. The steam was then forced through the turbines, much like the modern power stations (Hongwei Zhu *et al.*, 2011).

The biggest design obstacle was not in the power generation cycle itself, but that of the heliostat support structure. The optimum design structure was needed to drive down the cost of the system, since half of the construction cost of a solar thermal plant lies in the cost of the heliostat field. The trade-offs include the simplicity of the designs in order to drive down the costs of the high volume manufacturing modules versus the reliability and the durability of the structure to wind loads. Solar One produced 10 MW of electricity with a 72 650 m<sup>2</sup> heliostat surface area (Solarpedia, 2015).

In 1995 Solar One was modified and converted to Solar Two, by adding some more heliostats (82 750 m<sup>2</sup>) to also produce 10 MW of electricity during peak solar intensity, but also with storage available. The working fluid was also changed to molten salt, instead of water as in the case of Solar One. This increased the production time of the plant since the storage tanks had a capacity of three hours. Solar Two was declared a major success since this research led to developments of large scale solar energy projects. It was decommissioned in 1999 and converted into a telescope to measure the gamma rays hitting the atmosphere. The Solar Two project demonstrated the ability to use molten salt as a cost effective thermal energy storage system (Solarpedia, 2015).

## 1.3 Concentrated solar power in South African context

South Africa is currently implementing the largest renewable energy program in Africa, which makes it an exciting area for CSP. South Africa is looking to diversify its energy mix, since coal based power stations has been the predominant form of generation. The South African Government announced in December 2014 that it will be doubling the amount of power it intends to draw from the renewable sector, by increasing the bid

amounts (Fin 24, 2015). The Department of Energy awarded 13 new Independent Power Producers bids which increased the total renewable energy that can be supplied to the grid to 5 243 MW.

The South African Government currently relies on very old power stations to satisfy the energy demands, the oldest one being Pretoria West Power Station that was commissioned in 1952 (Matchdeck, 2015). The normal life span of a coal-fired power station is about 30 -35 years, Pretoria West Power Station is more than two decades past its lifespan. When this lifespan is used to determine the amount of “old” power stations still in operation by the end of 2015, the capacity accumulates to 9000 MW and increases to 15 600 MW by 2020. Not only are these power stations inefficient, but they demand a large amount of maintenance to keep them going. This means that almost 16 GW of new power supply units must be developed in five years’ time. These supply units make the renewable energy field such an important developing mechanism.

In South Africa there are currently seven CSP projects under development or construction. They consist of the Bokpoort Projects, Ilanga I, Kathu Solar One, Kaxu Solar One, Khi Solar one, Redstone Solar Thermal Power Plant and Xina Solar One. All of these projects are based in the Northern Cape where the highest solar radiation is available, which can be seen from Figure 2. Of all the projects, only one (Kaxu) is currently in operational phase, where all the others are still under construction (NREL, 2015).

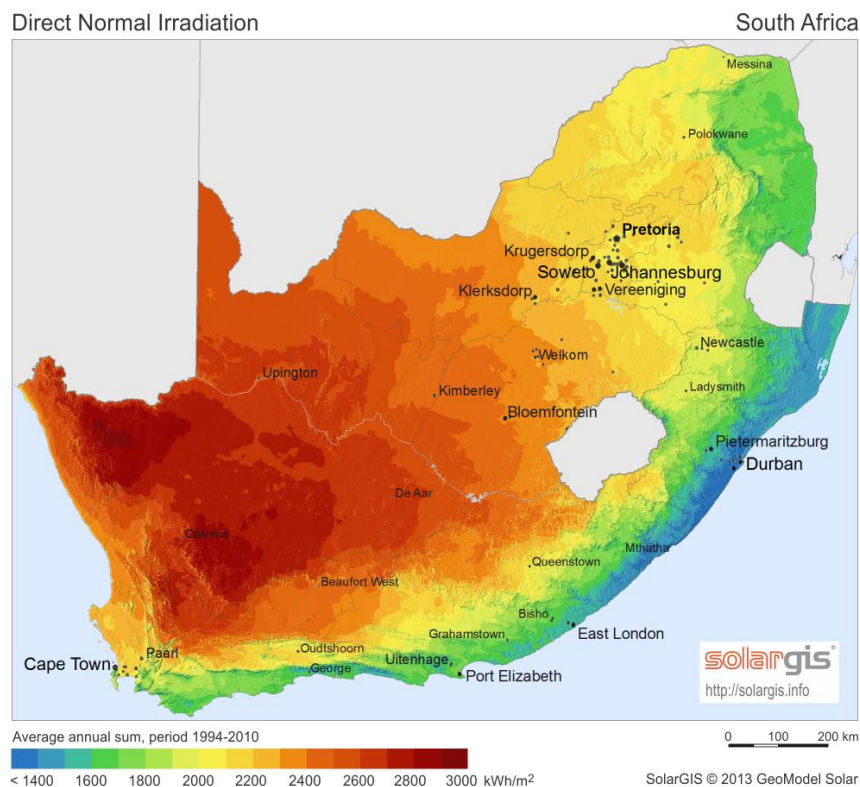


**Figure 2: DNI map of South Africa**

(Source: [www.geosun.co.za](http://www.geosun.co.za))

Table 1 below shows the current CSP projects and the status of each one (as on 1 April 2015), as well as some valuable information with regards to the technology used and storage capacities. It is evident that the parabolic through systems are the favourite among CSP in South Africa.

**Table 1: Update on the current CSP projects in RSA**

<b>Plant</b>	<b>Technology</b>	<b>Capacity</b>	<b>Status</b>	<b>Storage</b>	<b>Completion</b>
Bokpoort	Parabolic Trough	50 MW	Construction	9.3 hours	Dec. 2015
Ilanga I	Parabolic Trough	100 MW	Development	4.5 hours	2017
Kathu	Parabolic Trough	100 MW	Development	4.5 hours	2018
Kaxu	Parabolic Trough	100 MW	Operational	2.5 hours	March 2015
Khi	Power Tower	50 MW	Completed	2 hours	Dec. 2015
Redstone	Power Tower	100 MW	Development	12 hours	2018
Xina	Parabolic Trough	100 MW	Construction	5 hours	2017

Source: (NREL, 2015)

The renewable energy sector came as a life saver in terms of energy shortages, not to mention the financial or socio-economic benefits it has on the country. Even though all the CSP projects combined production is less than that of Matimba (Department of Energy, 2013), their influence in the greater scheme will still be small. Their impact will increase as more plants are commissioned.

#### **1.4 SUNSPOT**

The Stellenbosch University Solar Power Thermodynamic cycle (SUNSPOT) is a solar driven system that will be generating electricity through a solar thermal process. This system is ideal for South Africa due to the high solar radiation fluxes available, especially in the arid north-western part of the country. This system was initially developed by the late, Professor Kröger, but many studies in different fields are currently underway in order to achieve a feasible prototype.

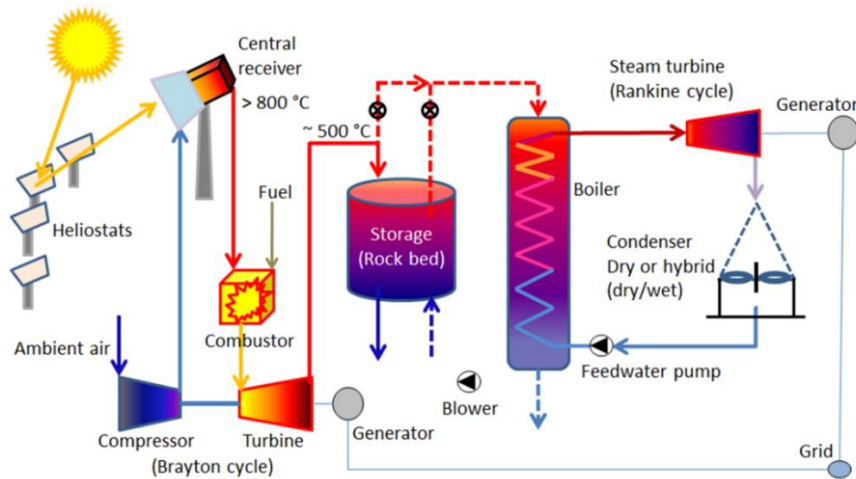


**Figure 3: The SUNSPOT cycle**

Source: (Kröger, 2011)

The basic lay-out of the system is shown in Figure 3. The receiver is situated between the compressor and combustor. The heliostats concentrate radiation from the sun onto the central receiver where the heat is transferred to the air. The aim of the solar receiver is to increase the air temperature before it runs through the combustion chamber. Fuel is burned in the combustor if the receiver outlet temperature is too low. Therefore a more overall efficient system can be developed if less fuel can be used.

Some of the unique features of the SUNSPOT system are that it uses a rock bed storage system, which stores thermal energy in the rocks. Not only are these rocks freely available, but they are also inexpensive to mine or produce and will have a longer effective operational time (from sunset to sunrise). The density of air is lower than that of molten salt, which will also in effect allow for smaller pump systems. By moving away from the popular molten salt system, solidification and corrosion risks are eliminated. Solidification can be overcome by using trace heat or draining heat exchanger, whereas corrosion can be eliminated by using high quality stainless steel structures. All these solutions have very high financial implications.

With the limited water availability for human consumption in South Africa, let alone the use for power generation, the government seeks more sustainable solutions to reduce the impact on the local water crises. The SUNSPOT system will thus make use of an air cooled condenser, which is one of the other big advantages, since water is normally scarce at locations with high solar potential.

With SUNSPOT still being under development, most of the research at the faculty is based on different components of the system. These studies range from receiver designs, storage alternatives, turbine designs etc.

### 1.5 Current pilot plants using air as working fluid

The first solar tower pilot plant that makes use of air as a working fluid was built in Jülich by the German Aerospace Centre and the University of Aachen in 2008. The plant consists of 2 153 movable mirrors with a surface area of nearly 18 000 m<sup>2</sup> and a

receiver capacity of 22 m<sup>2</sup>. The receiver is fixed on top of a tower which is at a height of 60 m above ground level (Funken, 2008).

The inlet air is at ambient temperature when entering the system and is heated up to 700 °C where the thermal energy is transferred to a water-steam heat exchanger. The steam generated by the boiler is used to generate a peak output of 1.5 MW electricity. The system also features a storage capacity which uses packed ceramic elements which is heated by the unused air. The system is then reversed once the storage facility is needed when clouds overhead are passing by.

The SOLUGAS project is the other pilot plant that made headlines, being the first hybrid power plant that makes use of fossil fuels and pressurized air. The system is capable of achieving outlet temperatures of up to 800 °C (Quero, Korzynietz, Ebert, Jiménez, del Río, *et al.*, 2014). Solar towers that do not use air as working fluid, like the Commonwealth Scientific and Industrial Research Organisation (CSIRO) project, have achieved much higher temperatures (up to 1500 °C) compared to air receivers (McGregor, 2014).



**Figure 4: The Jülich solar tower** (Source: <http://www.dlr.de>)

## 1.6 Overview of the designed annular solar air receiver

The solar receiver tube consists of a quartz tube, a copper pipe and an annulus filled with a porous medium that is called copper wool. This receiver tube is based on one of the tubes of the Hybrid Pressurized Air Receiver (HPAR) concept studied by Craig *et al.* (2014). This receiver developed, is unique due to a combination of specially designed features. The absorbing material has no structural function, whereas the outer glass tube will transmit the shortwave radiation and traps the long wave radiation. The porous medium has large heat transfer characteristics due to large surface area which

can release the heated air directly into the compressed air stream. The inner copper pipe will carry the load of the structure which is also cooled down by the inlet air that will improve the structural strength of the pipe. A single tube is tested in order to determine the properties of the porous medium and measuring the performance of an individual concept.

### **1.7 Research objectives and scope**

The core aim of this research project was to develop, test an air solar receiver tube and using the data to determine properties of the porous medium. The cost and area availability on the department's Sunroof Laboratory is the primary constraint in terms of the size of the setup. Due to safety considerations, the receiver will be tested at low temperatures and pressures. An emphasis was placed on the radiation properties of the copper wool, especially to determination of the absorption coefficient.

The aim of the experiment was to build a test rig to determine what areas of the receiver need to be investigated further. This means that a collector as well as a receiver needs to be designed and built. The experiment also tested the durability of the receiver since it was placed outside, exposed to all kinds of weather conditions. The test setup will be developed in such a manner that other receivers can also be tested without major modifications needed.

To summarize the objectives:

- Design receiver
- Design collector with tracking
- Install measuring tools
- Test receiver
- Create numerical Matlab simulation
- Do a CFD analyses
- Analyse data.

## CHAPTER 2. LITERATURE STUDY

An in depth study will be done on the different aspects of solar receivers. It will firstly give an overview of the different types of receivers available, followed by an analysis of the importance of some aspects, including pressure losses and receiver efficiency. The focus is then shifted towards the porous medium, where the radiative properties within the medium is analysed. The last part of the chapter focuses on the heat transfer within the whole receiver tube to determine critical sections in the system.

### 2.1 Different receiver types available

The modern research of receivers for central receiver systems is based on three different categories of solar receivers: gas receivers, liquid receivers and solid particle receivers. The classification of these receivers depends on the geometrical configuration and the absorber material that is being used. The general application of all three will be discussed, where a more in-depth study will be done on the gas receivers, since they are more applicable on the current study.

#### 2.1.1 Gas receivers

There are three different types of gas receivers used currently: volumetric air receivers, tubular receivers and cavity receivers. Volumetric air receivers consist of a porous medium placed inside a volume structure that is normally transparent to transmit the solar radiation. The solar energy is absorbed by the porous medium and then transmitted to the air that passes over it. The solar energy is firstly converted into thermal energy and then at a later stage to electrical energy by a turbine. These receivers were developed in the 1990's in various research projects (Hongwei Zhu *et al.*, 2011)

In the study done by Ávila-Marín, it was clear that much more research must be done on volumetric receiver before it will be commercialized i.e. the development of plant and control management strategies, the realibility of key components as well as the improvement of the material durability under high solar fluxes. On the other hand, closed-loop volumetric receivers show reasonable performance, the most promising one being, REFOS, the volumetric pressurized receiver for solar assisted fossil-fired gas turbine (Ávila-Marín, 2011), which can be seen in Figure 5.

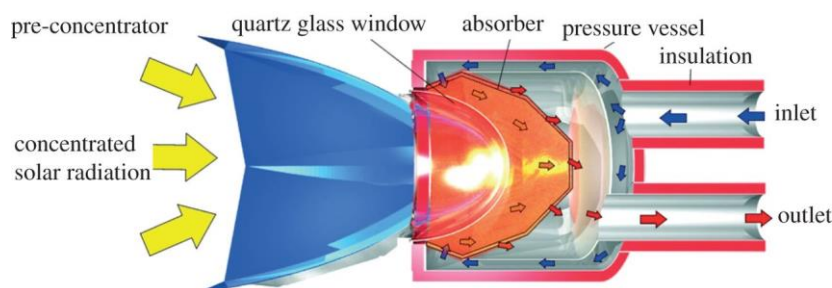


**Figure 5: The REFOS receiver**

(Source [www.solarenergyengineering.org](http://www.solarenergyengineering.org), accessed: 2016/04/18)

Results obtained by Hoffschmidt (2014) suggest that volumetric air receivers have the highest proven efficiencies (up to 80 %, plus) of the three. One of the major advantages of the volumetric air receiver is the low pressure drop from the inlet to the outlet, as a minimal pressure loss is most desirable in these systems. This will be described in more detail in the section to follow.

Tubular receivers are one of the most dominant receivers on the CSP market, whether it is for a parabolic trough, linear Fresnel or solar tower system. An example of a tubular receiver for a solar tower can be seen in Figure 6. Different working fluids can be used in tubular receivers, due to their less complicated geometric features. Therefore, the optimization of tubular receivers can be done more accurately and small variations could lead to major improvements in the system, compared to the volumetric receivers which have complicated geometric designs.

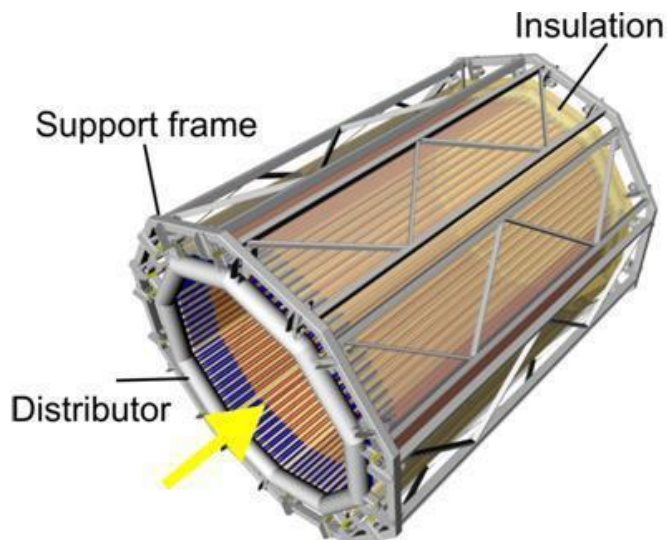


**Figure 6: Example of tubular receiver**

(Source [www.solugas.eu/index/overview.php](http://www.solugas.eu/index/overview.php), accessed: 2016/04/18)

### 2.1.2 Liquid receivers

Liquid receivers use tubular configurations to transport the working fluid which is mainly water/steam or molten salt. These two liquid receivers are the most matured technology available, but they are limited by the temperatures of the working fluid. Research by Forsberg et al showed that liquid sodium can be used as an alternative working fluid to increase the outlet temperature dramatically (Forsberg, Peterson & Zhao, 2007). Efficiencies in the range of 84-89 % appeared to be achievable in a study done by Singer *et al.* (2010).

A less popular receiver is the falling film receiver, which is driven by gravity fluid motion. As the fluid flows down the inclined wall, it can be heated by the wall itself or by the incoming concentrated solar radiation. This approach will reduce the pumping requirements a great deal, which will result in a more efficient system.

### 2.1.3 Solid particle receivers

Solid particle receivers are not as popular as the previously discussed receivers. This receiver uses solid particles, as the name suggest, absorbing the solar radiation from the heliostat field. A study from Hoffschmidt shows that there is no limit in the flux density which leads to high temperature power generation capabilities. In fact, the particles can be heated to temperatures higher than 900 °C (Hoffschmidt, 2014). These high temperatures can be obtained since the solar radiation is absorbed throughout the gas volume due to the large surface area present. Miller *et al.* (2000) confirmed in later studies that high efficiencies of up to 90 % can be reached with small particle receivers. These values depend on the different parameters like particle concentration, particle size, optical properties, mass flow rate etc. Development of a suitable window material and the development of a suspension system that will maintain an optimum particle concentration are among the major challenges researchers face in this field.

To conclude, Table 2 summarizes the receivers that were identified as possibilities. It is evident that there is no favourite, as each receiver will be used according to the different needs required.

**Table 2: Summary of receivers**

Receiver Type	Benefits	Challenges/Drawbacks
Volumetric receivers	Achieve high outlet temp. Flexible construction Large surface area for heat transfer Cheap working fluid	Material durability High radiation losses Low thermal efficiencies
Tubular receivers	Accommodate high pressures Low geometric complexity	Thermal expansion Material durability High radiation losses
Liquid receivers	High heat transfer abilities Has good storage capabilities*	Solidification problems* Fluid impurities Increase pressure requirements
Solid particle receivers	Direct radiation absorption Low flux limitations Cheaper than molten salt	Highest radiation losses of all types Low thermal emittance Extra heat exchangers required

\* Dependent on the working fluid

## 2.2 Importance of low pressure losses

The Brayton thermodynamic cycle represents the operation of a gas turbine engine which will be used in a gas driven solar plant like SUNSPOT. The first open hybrid system, for solar use, was developed in 2002 by DLR in Germany. The receiver is known as the SOLGATE receiver, which operated at temperatures of 960 °C to 1000 °C (SOLGATE Report, 2005). The inlet temperature at the turbine is a design constraint which is fixed due to material properties that can cause blade failure if it is too high. The open Brayton cycle can be seen in Figure 7.

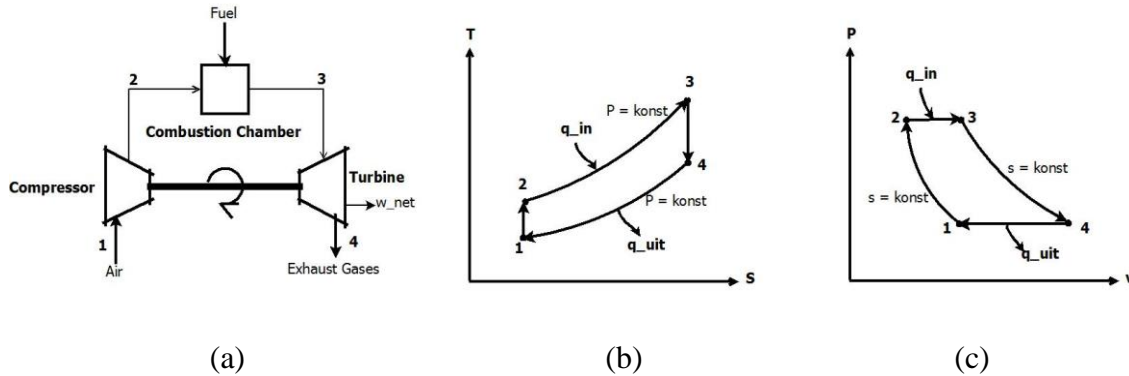


**Figure 7: The Brayton cycle**

According to Figure 7, it can be noted that the air is heated before it enters the gas turbine. This heating process increases the work output of the gas turbine at a specific air pressure. Air has poor heat transfer characteristics, which combined with the high heat fluxes associated with concentrated solar power, leads to material temperatures in the receiver substantially higher than the air temperature. Convection and radiation losses from the receiver at high temperatures can be significant and poses major challenges in the receiver design. Therefore the aim is to achieve the highest possible turbine inlet temperature at point 3 on Figure 7.

The thermodynamic efficiency for the cycle can be determined by using the fraction of the energy at the inlet of that of the outlet:

$$\eta_{th,Brayton} = \frac{w_{net}}{q_{in}} = 1 - \frac{q_{out}}{q_{in}} \quad 2.1$$

The enthalpy differences between the two sides can then be expressed as follows (if the working fluid is treated as an ideal gas with constant specific heats):

$$q_{in} = c_p(T_3 - T_2) \quad 2.2$$

$$q_{out} = c_p(T_4 - T_1) \quad 2.3$$

The thermal efficiency can then be expressed in terms of temperatures by combining equation 2.1 to 2.3:

$$\eta_{th,Brayton} = 1 - \frac{T_4 - T_1}{T_3 - T_2} \quad 2.4$$

To proceed further with the different efficiencies regarding the Brayton cycle, it is known that the points 1 and 4 are at the same pressure as is the case with points 2 and 3 on Figure 7 (c). Since both processes are at the same pressures, the following yields:

$$\frac{T_2}{T_1} = \left(\frac{P_2}{P_1}\right)^{\frac{(k-1)}{k}} = \left(\frac{P_3}{P_4}\right)^{\frac{(k-1)}{k}} = \frac{T_3}{T_4} \quad 2.5$$

This relationship can be substituted into equation 2.1 to give the thermal efficiency in terms of the pressure ratio ( $r_p$ ) between the low and high pressure.

$$\eta_{th,Brayton} = 1 - \frac{1}{r_p^{\frac{(k-1)}{k}}} \quad 2.6$$

This relationship proves that the efficiency of a Brayton cycle is not only temperature dependant, but also pressure dependant. In order to optimize the system, a highest possible outlet temperature is needed, with the least possible pressure losses between the inlet and outlet.

## 2.3 Radiation properties of participating medium

As radiation propagates through a participating medium, its intensity can be attenuated or augmented. This section will discuss the fate of radiation transfer in a porous medium as it passes through the receiver. Initially the absorption and scattering effect will be discussed as well as some terminology used, followed by the radiative heat transfer equation.

### 2.3.1 Radiative energy losses

Considering the spectral radiation intensity of  $I_{\lambda,0}$  entering a volume of length  $dx$  along the line of propagation  $x$ . As the radiation passes through the element volume, its intensity attenuates by means of absorption and scattering, as can be seen in Figure 8. This attenuation effect can be combined by a proportionality constant  $\beta_\lambda$  and the intensity can then be expressed by equation 2.7 (Howell & Siegel, 2011).

$$dI_\lambda(x) = -\beta_\lambda(x)I_\lambda(x)dx \quad 2.7$$

The proportionality constant is called the extinction coefficient of a medium, which includes both scattering and absorption of the radiation intensity. The extinction

coefficient,  $\beta_\lambda$ , depends on a variety of properties (temperature, pressure, material composition and the wavelength of the radiation) and has the unit of reciprocal length. If the specific medium is homogeneous, the extinction coefficient can be interpreted as the inverse of the mean penetrating length.

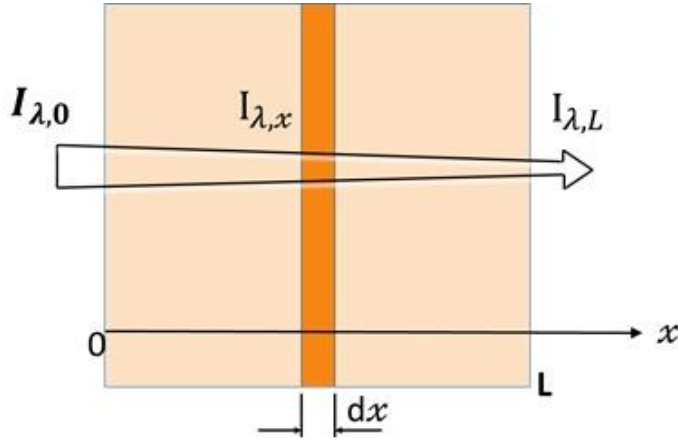


**Figure 8: Attenuation of the radiation**

The extinction coefficient can be divided into two separate coefficients, one for the scattering ( $\sigma_{s,\lambda}$ ) and another for the absorption ( $\kappa_\lambda$ ):

$$\beta_\lambda = \kappa_\lambda + \sigma_{s,\lambda} \quad 2.8$$

Both the scattering and absorption terms have also the unit of reciprocal length. The absorption term defines the conversion of radiation energy to thermal internal energy whereas the scattering take the direction change of radiation into account. In order to determine the energy decrease of the volume element, we have to integrate equation 2.7. By separating the variables and integrate from  $x = 0$  to  $x = L$

$$\int_{I_\lambda(0)}^{I_\lambda(L)} \frac{dI_\lambda}{I_\lambda} = - \int_{x^*=0}^L \beta_\lambda(x^*) dx^* \quad 2.9$$

where the incoming intensity on the control volume is  $I_\lambda(0)$  at  $x=0$ . The result is:

$$\frac{I_\lambda(L)}{I_\lambda(0)} = \exp(-\beta_\lambda L) \quad 2.10$$

If a medium is assumed to be absorbing only, the scattering term in equation 2.8 can be eliminated. The case when this can be assumed will be discussed in the chapter to follow. This modification is substituted back in equation 2.7 and the same integration can be done as above, to give:

$$I_\lambda(L) = I_\lambda(0)\exp(-\kappa_\lambda L) \quad 2.11$$

Equation 2.11 does not take any direction vector into consideration and is only viable for a uniform medium (Howell & Siegel, 2011). This phenomenon is better known as Beer's Law.

The next parameter that will be discussed is that of the mean penetration distance ( $l_m$ ). This is a very useful expression to use when analysing experimental data. The mean penetration length is obtained by multiplying the fraction of radiation absorbed at point  $L$ , by a distance of  $L$ . The next step is to integrate that over a path length from 0 to  $\infty$ .

$$l_m = \beta_\lambda \int_0^\infty x \exp(-\beta_\lambda x) dx = \frac{1}{\beta_\lambda} \quad 2.12$$

The same method can be followed if the analysis only takes scattering or absorption into account. However, replacing the extinction coefficient by either of the two will be sufficient for equation 2.12.

### 2.3.2 Formulation of radiative transfer equation

The spectral intensity refers to radiation with a certain wavelength ( $\lambda$ ), within an interval  $d\lambda$ , while the total intensity refers to the radiation within the whole spectrum of all wavelengths. This section will justify that the scattering term in equation 2.8 can be neglected which leads to equation 2.11.

As radiation passes through a medium on a path  $dS$ , it loses strength due to out scattering and absorption of the material, but it also gains additional strength due to out scattering from different directions, which end up on the same path as the current ray. The ray also gains strength from emission of other particles that end up in the same path length. This can be seen in Figure 9 for a specific frequency.

To determine the radiative transfer equation, the conservation of energy along a line of sight has to be written for a specific wavelength. A small element  $dV$  is considered with extinction coefficients, as explained above, and the scattering phase function ( $\Phi$ ). The energy equation is written in terms of a small solid angle  $d\Omega$  around the  $\theta$  direction within a small wavelength interval  $d\lambda$  at a constant frequency  $\lambda$ .

*The change in radiative energy = +Energy gain due to emission – Energy losses due to absorption – Energy losses due to the out-scattering + Energy gained due to in-scattering*

$$\begin{aligned} I_\lambda(S + dS, \Omega) - I_\lambda(S, \Omega) &= \kappa_\lambda I_{\lambda b}(S) dS - \kappa_\lambda I_\lambda(S, \Omega) dS - \sigma_{s,\lambda} I_\lambda(S, \Omega) dS \\ &+ \frac{1}{4\pi} \int_{\Omega=0}^{4\pi} \sigma_{s,\lambda} I_\lambda(S, \Omega_i) \Phi_\lambda(\Omega_i, \Omega) d\Omega_i dS \end{aligned} \quad 2.13$$

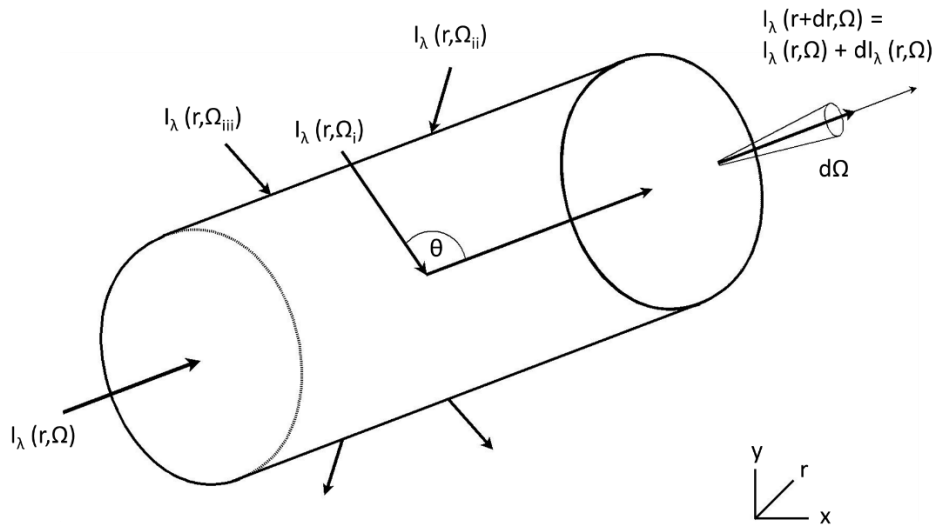


**Figure 9: Radiation propagating through a volume element**

The out-scattering of the rays in the porous medium never leaves the control volume, it only gets “absorbed” in the new direction. It then follows that the net change in the radiative energy on a path length  $S$ , equals the difference between the energy gained due to emission minus the energy loss due to absorption, since the scattering terms cancel each other out:

$$I_{\lambda}(S + dS, \Omega) - I_{\lambda}(S, \Omega) = \kappa_{\lambda} I_{\lambda b}(S) dS - \kappa_{\lambda} I_{\lambda}(S, \Omega) dS \quad 2.14$$

This proves that the scattering can be neglected for the specific configuration and the spectral radiation for absorbing only cases can be used as in equation 2.11 as done by Baillis and Sacadura (2000).

## 2.4 Porous medium studies

Different types of porous media have been investigated and tested in the past with the main objective to establish a viable option which can be applied in open volumetric receivers in solar towers to serve as the energy absorber. However, very few publications are available in the literature that discuss the experimental radiation testing of porous medium filled air receivers. There is, however, a large amount of research available with regards to different applications of porous medium within combustion technology as reviewed by Mujeebu *et al.* (2009). These studies look more into the heat transfer abilities than the radiation properties itself, since it consists of an interaction between a flammable gas and the porous matrix.

The research done by Fend (2010) on the capabilities of using porous medium in the Jülich tower provided some valuable information regarding the difficulties regarding the experimental testing of the porous medium. Fend proved that the hot spots that were

observed during the testing could be explained by theoretical analyses of the properties of the material. These include the conductivity and permeability of the material. The study suggested that a low cost receiver with a high durability and simplistic manufacturing process is needed to drive down the cost of air receivers. This study will be one of the main driving forces in terms of the specifications for the receiver.

In another study done by Fend, the author tested different materials experimentally to determine the properties of the materials. Foam ceramics, fibre mesh, ceramic catalyst and metal catalyst were among the tested materials. The best materials, according to their properties, were that of the ceramic foam and fibre. These materials have large specific areas combined with low pressure losses (Fend *et al*, 2004). The downside, however, is that they are very expensive, not freely available and complicated to manufacture.

### 2.5 Heat transfer analyses

The heat transfer model is based on an energy balance between the receiver and the environment. It will take the concentrated solar flux, the losses to the environment and the energy conversion into account. A two-dimensional analysis will be conducted to determine the losses in the system, since receivers with a length greater than 100 m will need a three-dimensional analysis (Foristall, 2003). This analysis will include all the necessary equations to solve the heat transfer problem in the Matlab model and also to determine the efficiency of the receiver.

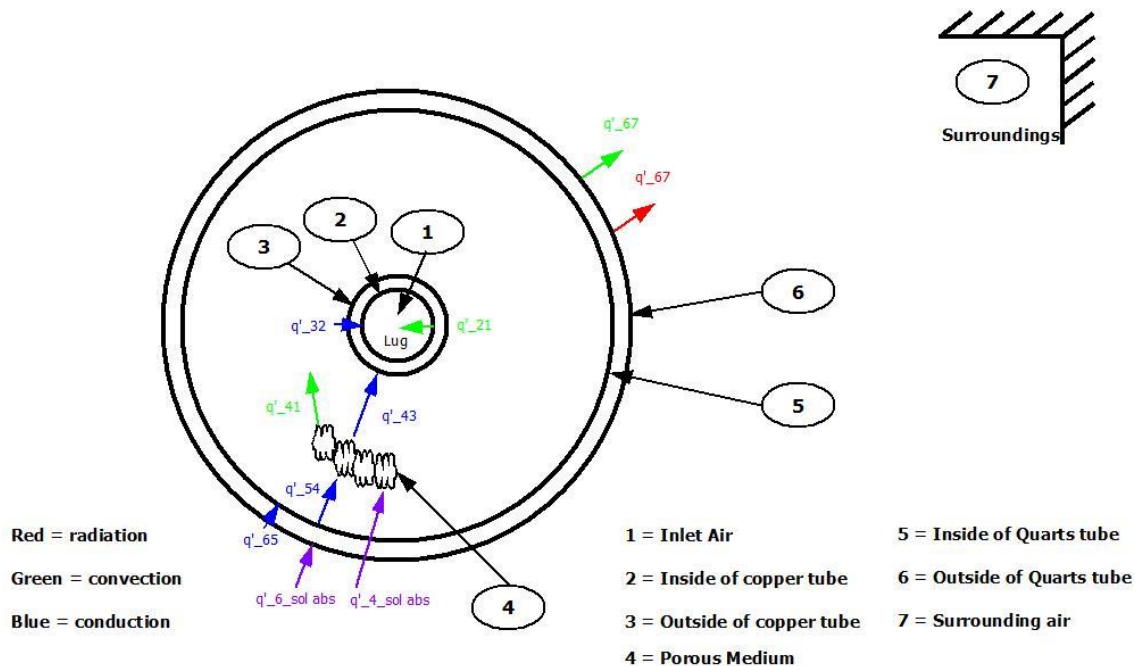


**Figure 10: Heat transfer diagram of receiver**

The heat transfer diagram in Figure 10 takes conduction, convection and radiation into consideration. These will not all be used at the same time for each model, since different analyses require different information. In order to determine the efficiency of the system, an analysis on the outer boundaries has to be done and is presented in equation 2.17.

$$q'_{heat\ loss} = q'_{conv,67} + q'_{rad,67} \quad 2.15$$

$$q'_{energy\ in} = Cr \cdot DNI \cdot D_{glass} \cdot \eta_{glass\ tube} \quad 2.16$$

$$\eta_{system} = \frac{q'_{energy\ in} - q'_{heat\ loss}}{q'_{energy\ in}} \quad 2.17$$

The spillage is neglected in the system which result that the diameter of the quartz tube is used to determine the net aperture, and not the mirror width. This is valid since the efficiency of the collector is not taken into consideration. The conduction analysis will be done later in CHAPTER 4, since this is just an overview of the setup. Before some of the heat transfer analyses will be described, the flow regimes will be evaluated for the different parts of the receiver.

### 2.5.1 Air flow analyses in the receiver

The flow analyses will be separated into two separate parts, first being the air flow through the copper pipe, which is straight forward, and the second being the outlet air as it passes through the porous medium.

The flow regime can be either laminar or turbulent. This will be determined by the Reynolds number which depends on the flow conditions. The Reynolds number is defined by the temperature dependant properties of the working fluid and the flow tempo thereof.

$$Re = \frac{\rho V_{avg} D}{\mu} \quad 2.18$$

The properties of the air will be determined at the bulk mean fluid temperature, which is the arithmetic average of the fluid temperature at the inlet and outlet of the different tubes.

$$T_b = \frac{T_{inlet} + T_{outlet}}{2} \quad 2.19$$

In the copper pipe, a relative precise Reynolds number calculation can be done to determine the flow regime, but once the flow starts to pass through the porous medium, assumptions will be made regarding the disturbances. Under most conditions, without any large disturbances, flow in a tube is laminar if  $Re < 2300$ , turbulent if  $Re > 10000$  and transitional if in between (Çengel and Ghajar, 2011, p.468).

The hydrodynamic entry length is the distance from the inlet to where the wall shear stress reaches within two per cent of the fully developed value. The flow will be assumed to be fully developed after this region. In laminar flow this value increases

linearly and reaches a maximum at a Reynolds number equal to 2300. The entry length ( $L_E$ ) for laminar and turbulent flows are as follows (Çengel and Ghajar, 2011, p. 471):

$$L_{E,lam} = 0.05 Re D \quad 2.20$$

$$L_{E,turb} = 10D \quad 2.21$$

It can be seen that the entry length is much smaller for turbulent flow than for laminar flow. This is due to the intense mixing during random fluctuations that usually overshadow the molecular diffusion effects. The hydrodynamic length will come in handy when analyses that are only applicable to fully developed flow are done.

The Nusselt number for internal, fully developed flow in smooth pipes can be determined by using Colburn's Equations, which is applicable for turbulent flow and heating. The properties of air will again be determined by using the mean bulk temperature of the air.

$$Nu_{int} = 0.023 Re^{0.8} Pr^{0.4} \quad 2.22$$

In order to determine the convective losses of the air receiver, the wind speed must be known as well as the temperature of the air and the surface temperature of the glass tube. The Nusselt number will change to that of equation 2.22 since the flow will be external and not internal. The Nusselt number can be determined by using the compact form of Churchill and Bernstein's formulation (Çengel & Ghajar, 2011):

$$Nu_{ext} = 0.193 Re^{0.618} Pr^{1/3} \quad 2.23$$

The air properties will be determined by using the film temperature which is the average temperature of the surface of the receiver and the surrounding air temperature.

$$T_f = \frac{T_\infty + T_s}{2} \quad 2.24$$

### 2.5.2 Convection heat transfer to the air

The convection analyses from the copper pipe, to the inlet air can be calculated by using Newton's law of cooling. This will be a very small amount and will be negligible in some analyses as the surface temperature at the outside of the copper tube will be assumed to be the same as the inlet air. This is only acceptable at low temperatures.

$$q'_{21_{conv}} = h_c D_2 \pi (T_2 - T_1) \quad 2.25$$

with the inside convective heat transfer coefficient ( $h_c$ ) being:

$$h_c = Nu_{int} \frac{k_1}{D_2} \quad 2.26$$

The Nusselt number will be calculated based on the inside diameter of the copper tube by using equation 2.22 and the convective heat transfer coefficient based on the thermal conductance ( $k$ ) of the inlet air. The temperatures that will be used are that of the average air temperature and the surface temperature of the copper tube. The convection analyses from the copper pipe to the outlet air through the annulus will not be considered since it will not be modelled in the Matlab model.

### 2.5.3 Conduction in the copper pipe

In some of the analyses, the outside temperature of the copper tube will be assumed to be the same as the inlet air, since the thermal conductivity of copper is 100 times more than that of air (large conductivity means small change in temperature). Equation 2.27 will also only be used to establish that the conduction in the copper pipe can be neglected at small pressures and temperatures.

$$q'_{32\_kond} = 2\pi k_{23}(T_2 - T_3)/\ln\left(\frac{D_3}{D_2}\right) \quad 2.27$$

The copper pipes that are being used is that of class one, with a thermal conductivity of 358 W/m K as listed in the plumbing code of practise (Copper Tubing Africa, 2015).

### 2.5.4 Convection and radiation losses from quarts tube to environment

As the energy is absorbed by the quarts tube and the porous medium, the surface temperature of the quarts tube increases, but at the same time emits energy through convection to the environment. This analysis will be critical in establishing the efficiency of the receiver.

$$q'_{67\_konv} = h_o \pi D_6 (T_6 - T_\infty) \quad 2.28$$

with the outside air convective heat transfer coefficient ( $h_o$ ) being:

$$h_o = \frac{k_{air}}{L_c} Nu_{ext} \quad 2.29$$

The external Nusselt number can be calculated by using equation 2.23 and the thermal conductivity of air will be determined by using the film temperature. The outside sky temperature represents  $T_\infty$  and the temperature of the copper pipe  $T_6$ . It will be assumed that the sky temperature and the surrounding temperature is the same, since the tube

radiates heat towards the surrounding structures. This assumption is viable since radiation losses are small at low temperatures.

The other losses in the receiver to the environment are as a result of thermal radiation. As the energy is emitted from the sun it will be either transmitted through the glass ( $\tau$ ), absorbed by the glass ( $\alpha$ ) or it will be reflected ( $\rho$ ) as it strikes the surface.

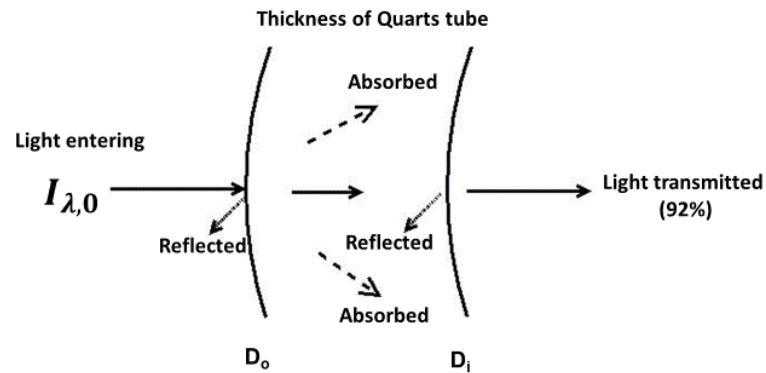


**Figure 11: Absorption, reflection and transmission by porous medium**

By assuming that the receiver is a small object in a large cavity (environment), the view factor can be regarded as unity which leads to the energy emitted as:

$$q'_{67_{rad}} = \sigma \varepsilon_{glass} \pi D_{o,g} (T_6^4 - T_\infty^4) \quad 2.30$$

where  $\sigma$  is the Stefan-Boltzmann constant and the area is determined by the outer diameter of the quartz tube.

## CHAPTER 3. DESIGN, SETUP AND CONSTRUCTION

The following section will focus on the design aspects of the system, which includes the different tracking methods considered as well as a detailed description of the receiver itself. A complete experimental setup is given to ensure that all the vital procedures are described. Some structural analyses are given to verify that the structure will not fail during testing, which can cause injuries.

### 3.1 Support and collector structure

The support structure of the solar air receiver consists of a rotational base, with the two vertical steel pillars to support the receiver and a detachable steel structure where the mirrors are fitted on. The support structure is made from 32 mm steel square tubing that is more than capable of carrying the weight of the receiver and the collector structure without having large deflections. A CAD model of the structure can be seen in Figure 12. High wind loads were not considered for deflection purposes, since testing at high wind speeds will be avoided, in order to minimize the uncertainties. The structure will, however, be able to accommodate high wind speeds without failure to any components.

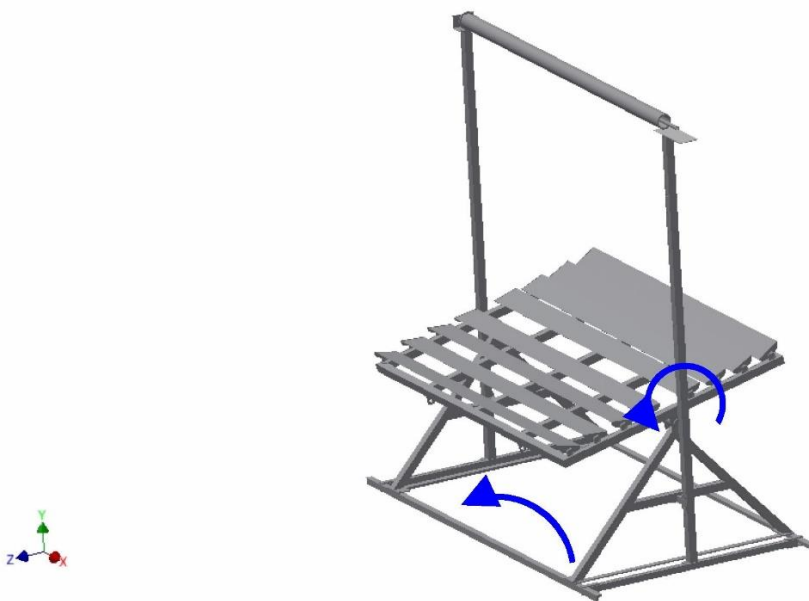


**Figure 12: The support structure with receiver**

When a structural analysis is done on the structure supporting the mirrors, it can be seen that a small deflection of 1.4 mm is present at the endpoints of the beam, whereas the deflection angle is less than 0.20 degrees. It is clear that these deflections will not have any effect on the system after the mirrors are calibrated. These calculations can be seen in APPENDIX B. The formulas used for a cantilever beam with a uniform load, fixed at the middle of the beam are displayed in Figure 13 accompanied by equation 3.1 and 3.2.

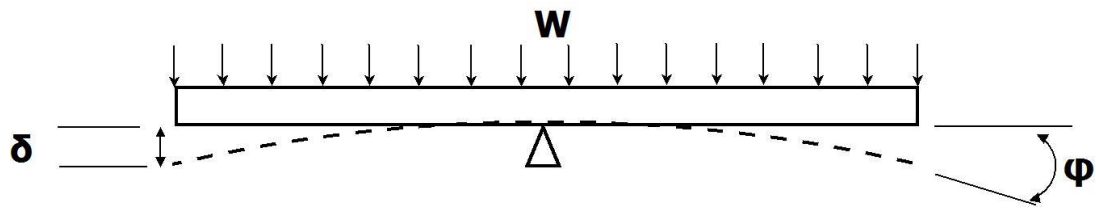


**Figure 13: Structural analyses of the beam**

$$\delta_{max} = \frac{5wl^4}{48EI} \quad 3.1$$

$$\varphi_{max} = \frac{wl^3}{24EI} \quad 3.2$$

The eight mirrors used, 1400 mm in length and 100 mm wide, are commercial glass mirrors that are freely available at any retailer. Only eight mirrors were chosen due to the large cosine losses that will be present if the concentration ratio is increased. Since the outcomes of the project does not take the optimization of the project into consideration, the type of mirrors were chosen due to their price and availability. The biggest obstacle in CSP plants is to minimize the cost of the collector fields which also led to the idea of using low cost mirrors instead of low iron mirrors.

The mirrors were also fitted on top of a 3 mm thick plate which will carry the load of the mirrors to avoid bending at the centre. This is vital since a constant heat flux is required on the receiver tube. A non-uniform flux will cause hot spots in the material which might cause failure or inaccurate measurements. The mirrors were fixed on the flat plate with a special bonding that can handle the thermal expansion during testing and also extreme weather conditions like rain and high speed winds.

The mirrors were placed in such a position that very little to no shadow effect will be present on the mirrors, which mean that shading losses can be neglected since testing will only take place during peak solar periods. The mirrors were also over designed in the sense that the cosine effect will not have an effect on the system. These design specifications were put in place in order to simplify the analyses and to develop a cheaper tracking system.

The receiver was placed at a height of two meters above the ground. This design constrain was due to safety issues which incorporate the maximum height the receiver can be, while working at ground level. In addition, the higher the receiver is placed, the more sensitive it is to small changes in the tracking system.

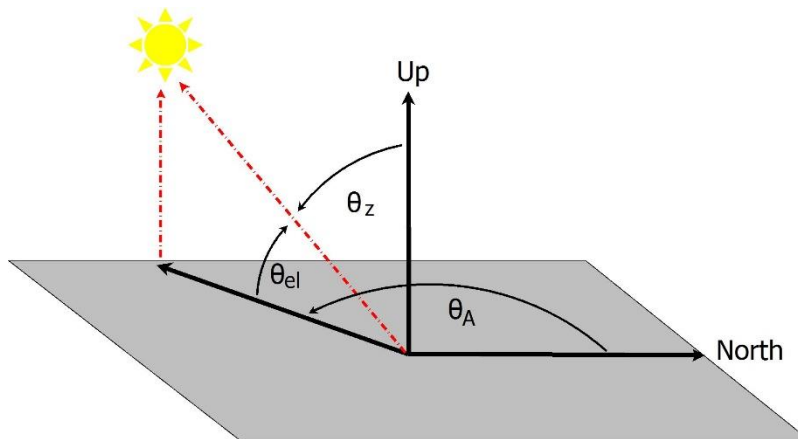


**Figure 14: Sun position angles**

In order to establish the position of the sun, a coordinate system has to be specified. The elevation angle ( $\theta_{el}$ ) is measured from the horizon, being “zero” after sunset whereas the zenith angle ( $\theta_z$ ) is measured from the vertical and the azimuth angle ( $\theta_A$ ) measured from the North.

Using the sun’s position and the latest possible time when testing can take place, the pivot point height of the mirror support structure (from the ground to centreline of mirrors) was designed to be 0.6 m from the ground. This is not a vital dimension, since a normal test will take approximately 20-40 minutes and not a whole day, but gives an estimate of the size of the collector which can be seen in APPENDIX E.

The direct normal irradiance (DNI) for one of the testing days can be seen in Figure 15 (Sonbesie, 2015). It is clear that the majority of the testing must be done between 10am and 3pm in order to test in the top 90 % of DNI levels. This will have smaller DNI variations over time and a more consistent reading. The sun’s elevation angle was between 40 and 75 degrees during that time period of testing.

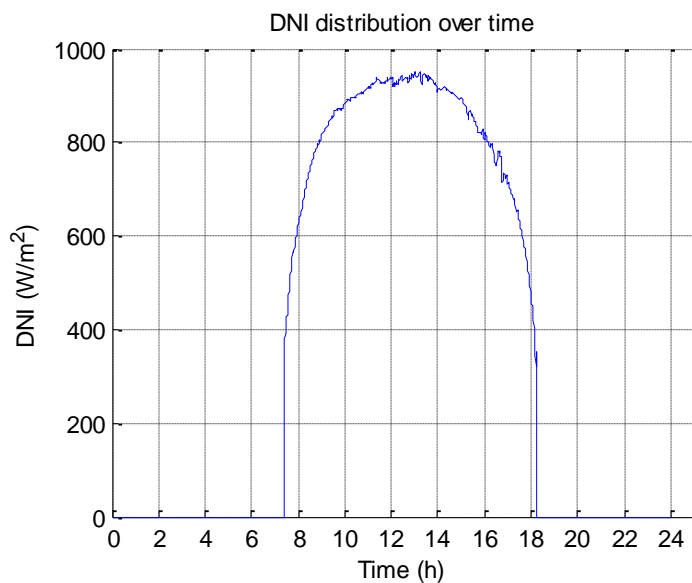


**Figure 15: DNI distribution for the 30<sup>th</sup> of March 2015**

### 3.2 Tracking

The tracking of the system is an important aspect, not only in terms of the performance of the system, but also in terms of the financial implications. Both of these constraints had been taken into account when the tracking mechanisms were designed. The two mechanisms that were considered, were manual and automatic tracking. The tracking can also be single axis or double axis, as can be seen from Figure 16. The pros and cons of the different systems will be discussed next.

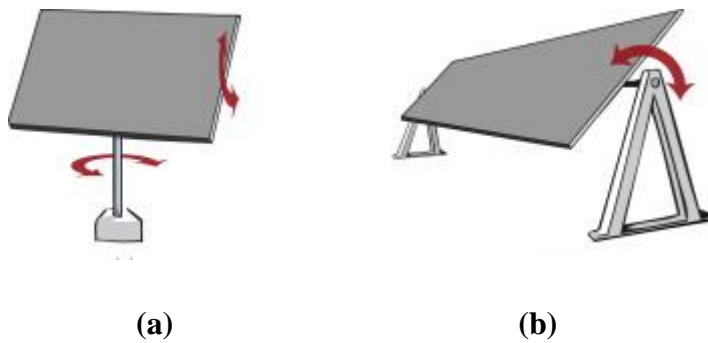


**Figure 16: Multi axis and single axis tracking**

A single axis tilting system, like the one in Figure 16(b), is the easiest and cheapest one to install. These systems are normally installed on parabolic trough systems, which have more or less the same configuration setup as this study, except they are much longer in length.

The two axis tracking system, like the one in Figure 16(a), is more complicated and significantly more expensive. These systems are used on heliostats with solar towers or in concentrated photovoltaic systems. The advantage of this tracking mechanism is that all the reflected energy can be used, since there are few spillages or losses. This is, however, not the case with a single axis tracking system, where there is plenty of spillage when tests are done in the early mornings or late afternoons.

If an automatic two axis tracking system is installed, accurate close loop motors will be needed with very little backlash in the gears. Such a system will also need a very well programmed tracking software. An automatic single axis tracking system will probably be a better option when the time, application and budget are taken into consideration. Only a single linear motor will be needed for the tilting, since there will be no rotation. This control system is much easier to program than the two axis system.

A manual tracking system is much less complicated than an automatic system, if designed well. They require more labour during testing but will be sufficient for short testing periods and small scale models as in this study.

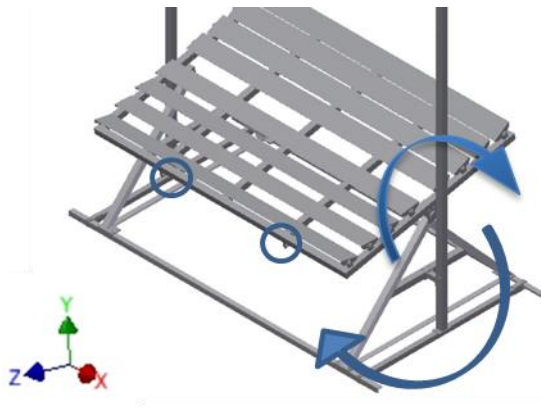


**Figure 17: Double axis tracking mechanism**

Taking all the above mentioned into consideration, a two axis, manual tracking collector will be used to concentrate the irradiation on the receiver. It was decided that an automatic tracking system will be too expensive and does not fit in the scope of the project, since a low cost system was developed. The single axis automatic tracker will give inconsistent irradiation measurements on the receiver and will thus not be suitable. The best option will be to overdesign the mirrors, with as much as 60 %, to compensate for manual tracking errors, which will require the system to be adjusted at least every 2 minutes during testing.

The tilt angle will be adjusted (every two minutes) by a double threaded turnbuckle which is connected by cables at the circles in Figure 17. This adjustment will be needed to keep track of the elevation angle of the sun. The bottom base is placed on a circular track with wheels attached to it which is adjusted every time the tilt angle is adjusted. This will allow the collector to track the sun in the azimuth angle.

Since a manual tracking system is not a closed looped system, a continuous calibration mechanism is needed. This was done by means of a small tube attached to an L-bend plate. This tracking sensor is fixed at the centre of the collector, which can be adjusted each day before testing. Once fixed and calibrated for the day, it will be used to optimize the tracking. If a round sun-light circle is visible on the bend of the elbow, it means that the receiver is in the correct position. As the sun changes position, the circle becomes an ellipse shape and the collector needs to be adjusted. This tracking sensor can be seen in Figure 18.

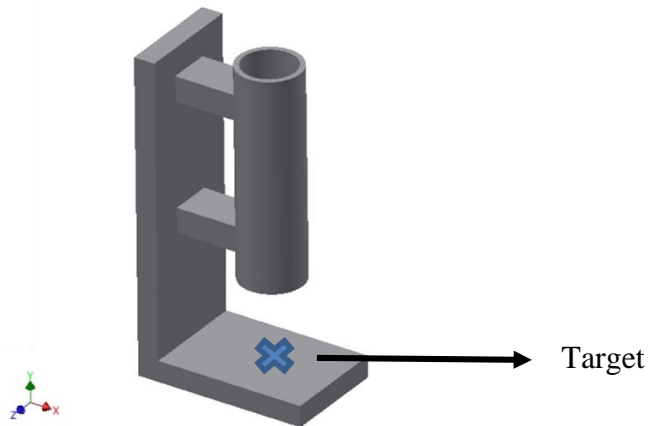


**Figure 18: Tracking sensor**

### 3.3 Receiver design

The solar receiver consists of a quartz tube, a copper pipe and an annulus filled with a porous medium that is called copper wool. This concept was developed from the different studies discussed in CHAPTER 2 and all of its components, as well as the air flow path, can be seen in Figure 19.

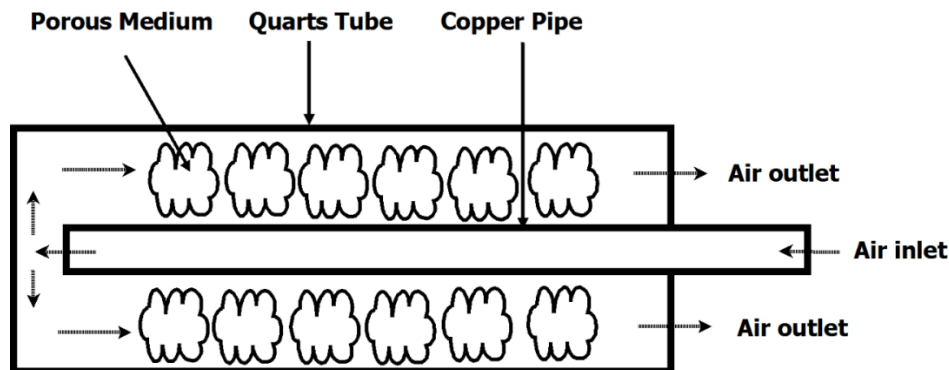


**Figure 19: Vertical cross section of receiver**

Air enters through the inner tube (on the right side of Figure 19), turns through 180° at the left hand side, and returns through the annulus which is filled with the porous medium. The outer quartz tube allows short-wave irradiation to penetrate and heat the opaque contents of the tube, whilst long-wave emitted re-radiation is trapped inside the tube, reducing radiation losses to the environment. This makes quartz tubes ideally suitable for receivers in the field of photochemistry.

The annular space is filled with a porous medium that absorbs solar radiation and at the same time offers a large surface area for heat transfer to the air. The porous medium that has been used is called copper “pot scourers”, which is available at many supermarkets. The irregular shape of the porous medium should ensure a high heat

transfer coefficient, keeping the material temperatures in the porous medium low. The pressure losses within the annulus will be minimal because of the specific configuration of the copper wool. Unequal thermal expansion of the two tubes and bowing under one-sided irradiation is also taken up by the porous medium.

Cold air enters through the inner metallic tube, keeping it cool and further ensuring structural integrity. The copper tube will therefore play a vital part in carrying the loads of the structure.

### 3.4 Final experimental setup

The complete receiver design, while being tested can be seen in Figure 20 below. The Department has a central tank for the compressed air (at 10 bar) where it is then transferred to the experiment. This pipe is then connected before the pressure regulator where the air enters the system.

After the assembly process was completed, the mirrors had to be calibrated on the receiver. This was done by having centre red markers on the middle of each of the two ends. These red marks resulted in a shadow that can be seen on the receiver. All the mirrors had to be calibrated individually which means every mirror have to be covered except the one being calibrated.

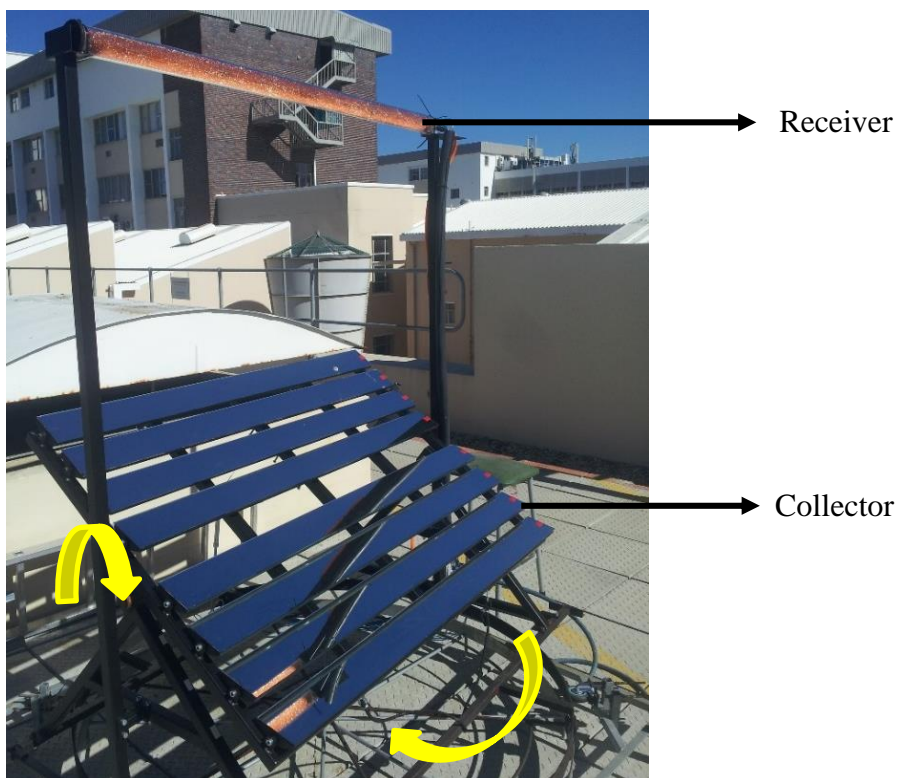


**Figure 20: Complete receiver design setup**

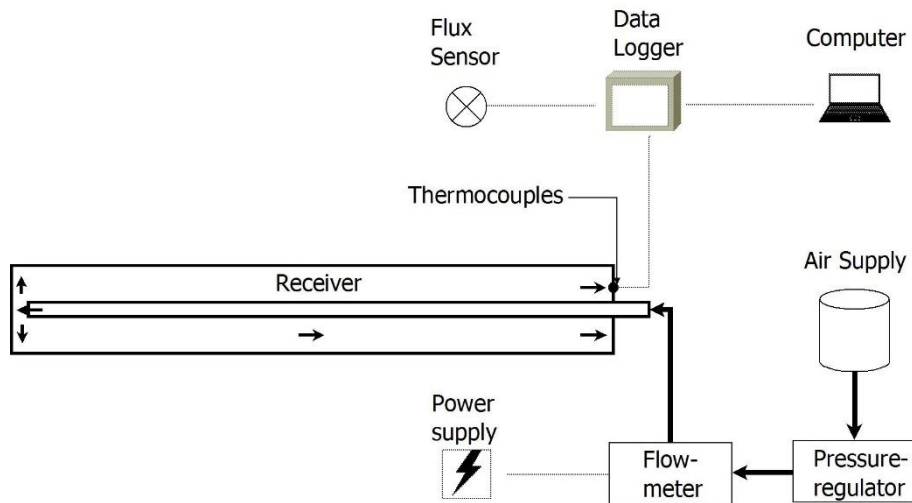


**Figure 21: Experimental setup**

The experimental setup of all the connected parts can be seen in Figure 21, with the solid black line showing the pipe transporting the air to the receiver and the fine lines the cable connections between the different instruments. A description of all the instruments and how the data will be gathered follows in Chapter 3.5.

### 3.5 The method

This study focusses on the radiative properties of the porous medium when it is in the receiver. Temperature measurements will be used to determine the amount of energy that has been transferred to the air, as well as the losses to the environment. This section will also strive towards clarifying any uncertainties in the results obtained and will form the back-bone for future studies on this receiver.

#### 3.5.1 Research designs

The best method to determine the temperature increase in the system is to do a field experiment, where the receiver is tested under normal conditions which include natural convection and radiation losses. This will however increase the amount of variables compared to an indoor test with artificial lights, where external radiation will be minimal compared to convection losses (when tested at relatively low temperatures  $<100\text{ }^{\circ}\text{C}$ ). Doing indoor tests will eliminate the nature variables, in terms of when testing can be done. Since Stellenbosch has a winter rainfall season, all tests must preferably be done during the summer months.

Another research design that will be used is that of a computational fluid dynamic (CFD) simulation. Test results and simulation results can be compared with each other to validate the system. The CFD analyses will also incorporate convection, which was not possible with the numerical Matlab model. In order to run the simulation, many assumptions had to be made, which can have an influence on the validity of the simulation.

### 3.5.2 The methodology

This section will strive towards describing the exact procedure if the experiment was repeated. There were different instruments used in order to gather the data. It ranges from data loggers, to flux sensors and flow measuring devices. These instruments were all calibrated before the data was recorded. An instrumental list can be seen in APPENDIX A with the different models listed.

The data logger was used with thermocouples to measure the temperature at the outlet of the annulus. There were four different parts identified in the receiver where temperature measurements needed to be taken, as can be seen in Figure 22. These areas were identified as critical areas where the most activity happens. The thermocouples were placed in sets of three and at the same radial distance from the centre. They are spaced equally apart from each other in the radial direction. This means that when we consider section 1 in Figure 22, the distance from quartz tube to the top thermocouple is the same as from the top thermocouple to the centre thermocouple etc.

The potential differences/voltages of the thermocouples were logged every five seconds by the data logger. Knowing the properties of the thermocouples, the voltage readings were converted to a temperature reading. These converted readings were then used to plot the temperature profile over the the radial distance.

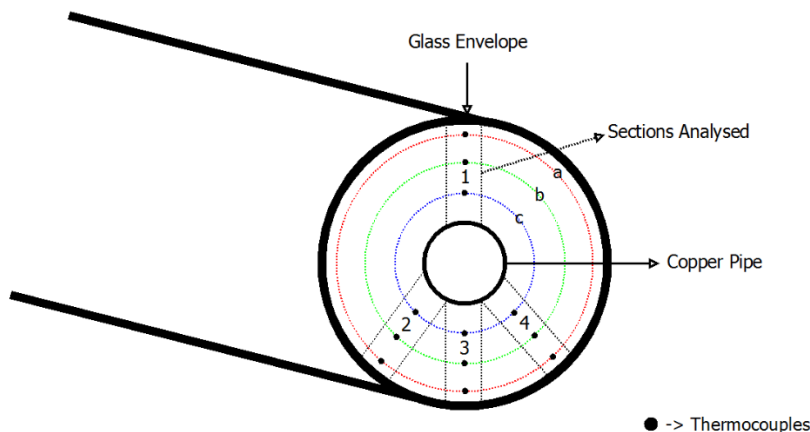


**Figure 22: Placement of the thermocouples**

The experimental setup will make use of the Departments' solar and weather station, Sonbesie (2015), which is situated on the roof near the setup. The Direct Normal Irradiance (DNI) will be gathered for the concentrated flux calculations, whereas the wind speed and the ambient air temperature will be used to determine the losses to the environment.

The next instrument used, were the solar flux meter. It works on the same principle as a thermocouple which also gives a measured voltage reading as an output and can then be converted to a solar flux reading with a known thermal conductivity value ( $k$ ) and distance between two measured points ( $\Delta x$ ). This explanation can be seen in equation 3.3. This tool was only used during the calibration of the setup and not during the testing period, since it will result in a shadow on the receiver.

$$\frac{Q}{A} = -k \frac{\Delta T}{\Delta x} \quad 3.3$$

The solar flux meter was used to measure the concentrated flux at the receiver. With a fixed concentration ratio of 8, a known mirror efficiency and a DNI reading (through the M&M weather station on the roof), the solar flux was calculated and compared to the measured one. This part of the calibration ensured that an accurate calculated concentrated flux can be determined by only using the DNI reading from the weather station. The concentrated solar flux was measured at three different points on the receiver to validate the calibration of the mirrors.

Note that both the flux meter as well as the thermocouples are connected to the same data logger, which is in turn connected to a computer to write all the measurements on the hard drive. This will guarantee that the data is synchronized with each other.

The flow meter and the pressure regulator worked in tandem. The volumetric flow rate was identified as the dependent variable and the pressure controlled by the pressure regulator, the independent variable. The setup was tested for two different pressure ranges, the first being a low pressure, which means low flow rate, and the other being a high pressure, high flow rate case. After those tests data were gathered, the pressure was set at a constant rate to eliminate another variable in the system. The pressure regulator have an upper absolute pressure limit of 100 kPa, which will be the maximum pressure under which the system can be tested. Due to safety considerations, this maximum pressure will be acceptable and within the design limits. An external power supply was needed to deliver power to the flow meter at a 24 V DC rating.

The surface temperature of the quartz tube will also be needed to calculate the radiation losses. A FLIR (model: E60) infrared thermal camera was used to take these measurements. The camera determines the temperature of a surface by means of an emissivity input of the material into the camera.

To conclude the general experimental test setup, the instruments had been connected as in Figure 21, and the following steps were followed:

- Step 1. Calibrate all equipment (refer to APPENDIX C)
- Step 2. Switch on the computer, power supply and data logger.
- Step 3. Set the pressure by the pressure regulator
- Step 4. Take the volumetric flow rate
- Step 5. Focus the collector on the receiver.
- Step 6. Start the logging of the data (Temperature measurements)
- Step 7. Change the focus of the collector on the receiver every minute.
- Step 8. Wait till the system reached steady state, which can be seen on computer, stop the temperature logging
- Step 9. Take photo with FLIR camera of surface temperature distribution.

- Step 10. Get solar and weather data from weather station.
- Step 11. Wait for system to cool down.
- Step 12. Change a variable and repeat test, starting at step 2.

The next research design that will be discussed is the computational fluid dynamics (CFD) simulation that will be done. The software that will be used is Fluent, which is licensed under ANSYS. A more in depth analyses of the model will be discussed later in Chapter 4.4, only the methodology will be discussed here.

The CFD analysis will be used to determining whether the scattering term can be neglected in the porous medium analysis. The CFD model strives towards creating a better understanding of how the system behaves, by giving information that is difficult to measure. A model of the receiver will be designed with the built in modelling software, where it constructs meshes using quad cells. The boundary conditions were assigned at the different inlets and outlets as well as the material properties. The absorption coefficient will be varied in the model to match the temperature outlet compared to the experimental setup, i.e. you use CFD as a tool to “fill in” missing information from your experimental set-up.

The results of a CFD simulation are extremely powerful in terms of the information that is available. The model can display a wide range of temperature distributions to pressure losses in the system, but the most important result is the temperature profile over the radial distance.

### 3.5.3 Data

After the completion of the test, the following data will be available:

- An array of the different thermocouple readings for each time step
- An array solar and weather data for each time step
- A constant pressure and volumetric flow rate
- Surface temperature distribution of quartz tube at steady state
- All calibrated data

The thermocouple calibration, as explained in APPENDIX C, determines the error for each thermocouple by using a calibrated reference thermocouple. This reading is converted from a voltage to a temperature as well as the array of measured voltages while testing. The error in the calibration calculations is then added or subtracted from the test data to achieve a more accurate temperature. The temperature profiles over the radial distance to the centre, for each of the identified sections, were then plotted.

The solar data that was downloaded is used to determine the solar flux on the receiver at each time step, which is the amount of energy that enters the system. The wind speed is gathered from the weather measurement, which will be used to calculate the convective losses of the receiver. The sky temperature as well as the average surface

temperature of the receiver will then be used to calculate the radiation losses from the receiver to the environment

The volumetric flow rate will be used to calculate the net heat transfer to the air, which will finally give the efficiency of the receiver with the rest of the calculation. The flow meter will be combined with the pressure regulator to determine the pressure losses in the system.

### 3.5.4 Analyses

The biggest obstacle regarding the project is to determine the absorption coefficient of the copper wool as well. The radiation properties of this non-uniform mesh make the analytical calculation of a three-dimensional problem nearly impossible, but with the help of experimental and simulation results, the problem can be solved. The analytical solution is unsolvable since the variables cannot be separated.

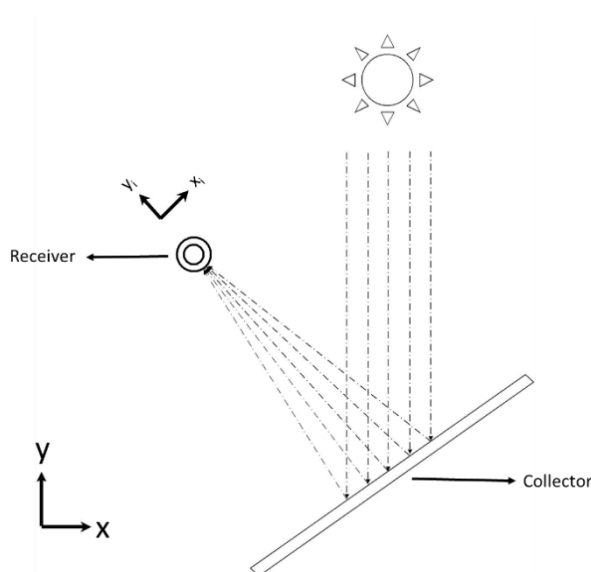


**Figure 23: Two different axes used for setup**

It follows that a temperature over radial length graph will be constructed of the different sections in the experimental setup, as well as the temperature profile of the simulated results. These results will be compared and modifications will be made to the absorption coefficient in the simulation model. This variable will be changed until the two graphs show a matching trend when a least square method is adopted. The end absorption coefficient will be the final determined value.

### 3.5.5 Conclusion

By following the described method, the test can be repeated without any difficulties. It is important to take note of the two different axis systems that is used during the overview of the setup. To conclude, the  $x, y, z$  axis is the global axis system and the  $x_1, y_1$  axis is the local axis system, as can be seen from Figure 23.

## CHAPTER 4. SIMULATION OF RECEIVER

The receiver will be simulated in two different manners, the first will be a finite difference model that will be coded in MATLAB, whereas the second simulation will be constructed in ANSYS. Both of these models will be discussed in depth, with all the necessary formulations given. Note that throughout the chapter, the numerical model will refer to the MATLAB model and the simulation will refer to the CFD model in ANSYS.

A cylindrical coordinate system will be used in chapter 4, as given in Figure 24. The axis normal to the plane will be the z-axis and the x and y coordinates can be determined as follows:

$$x = r \cos(\theta) \quad 4.1$$

$$y = r \sin(\theta) \quad 4.2$$

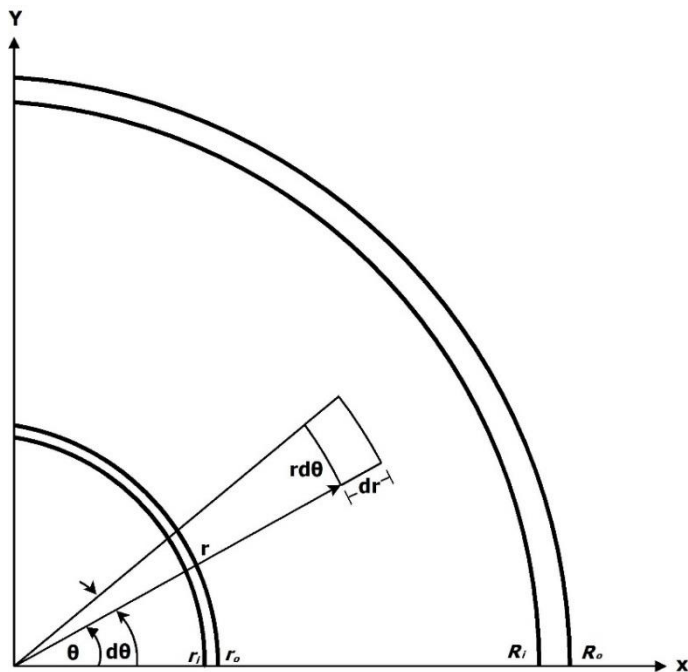


**Figure 24: Cylindrical coordinate system that will be used**

Throughout the chapter a consistent configuration will be used for the different pipe sizes,  $r_i$  will be the inner radius of the copper pipe and  $r_o$  the outer radius. Capital letters will be used to describe the outer quart tube, with  $R_i$  being the inner radius and  $R_o$  being the outer radius. This can be seen on the x-axis of Figure 24.

### 4.1 Assumptions in the numerical Matlab model

In order to build a numerical model, a few assumptions have to be made. The assumptions strive towards simplifying the model, without neglecting major effects. Due to the different methods in constructing the model, some of the assumptions will differ between the Matlab model and the simulated model. However, the variations in the model will be kept to a minimum required. The minor assumptions are as follows:

- The model will be evaluated at steady state.
- The reflecting efficiency of the mirrors is 82 % (info from manufacturers).
- Outside of copper pipe = inlet air temperature
- The rays entering the control volume will be parallel to each other.

The most important assumption that was made, was that the Matlab model assumes that conduction dominates convection in the radial direction. It follows that the model also assumes the air and the copper wool as a single material with an effective conductivity as was done by (Aichmayer, 2011; Mahmoudi & Karimi, 2014; Roldán *et al.*, 2014).

It was also assumed that a linear temperature profile is present in the length of the tube (z-direction) which result in  $dT/dz \ll dT/dr$  as done by Kays *et al.* (2004).

## 4.2 Energy equation background

Before the numerical model can be discussed the derivation of the discrete equation must be derived and explained in order to reiterate the importance of the absorption coefficient. The volume element of part of the solid is given in Figure 25, where the conduction in the z – direction (from the bottom to the top) is neglected.

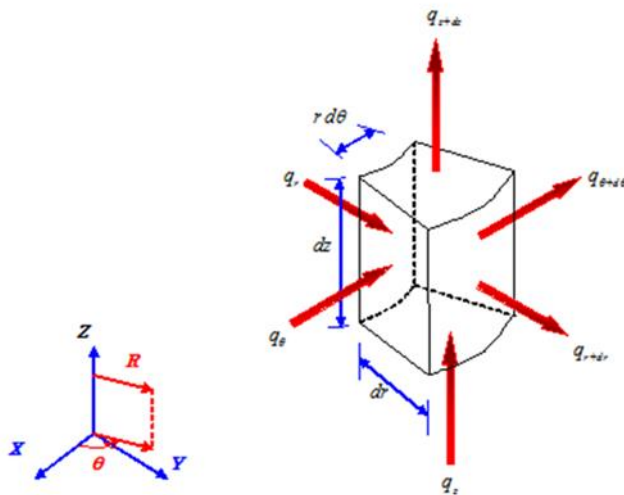


**Figure 25: Cylindrical volume element**

Credit: [www.intechopen.com](http://www.intechopen.com)

In general the temperature variation is in all three directions, but for this specific application, the conduction in the z-direction is neglect for the two-dimensional case and the conduction in the z and  $\theta$  direction is neglected for the one-dimensional case.

According to Fourier's law of conduction:

$$\mathbf{q} = -k\nabla T \quad 4.3$$

Combine equation 4.3 with the energy conservation principle and introduce an internal heat generation term, to re-write it into the form of convection = diffusion + source term:

$$\rho c u \frac{dT}{dt} + \rho c v_r \frac{dT}{dr} = \mathbf{q} + \dot{Q}_v''' \quad 4.4$$

When equation 4.4 is written in terms of the cylindrical coordinates, as described in Figure 25:

$$\rho c u \frac{dT}{dt} + \rho c v_r \frac{dT}{dr} = \left[ \frac{k}{r} \frac{d}{dr} \left( r \frac{dT}{dr} \right) + \frac{k}{r^2} \left( \frac{d^2 T}{r^2 d\phi^2} \right) + k \left( \frac{d^2 T}{dx^2} \right) \right] + \dot{Q}_v''' \quad 4.5$$

If this problem is restricted to symmetrical heat transfer ( $d^2T/d\phi^2 = 0$ ), hydrodynamic fully developed flow ( $v_r = 0$ ), no convection and we neglect axial conduction relative to radial conduction ( $d^2T/dx^2 = 0$ ), the energy equation for fully developed flow can be achieved with equation 4.5 to be (Kays *et al.*, 2004):

$$\frac{1}{r} \frac{d}{dr} \left( k \frac{dT}{dr} \right) + \frac{1}{r^2} \frac{d}{d\theta} \left( k \frac{dT}{d\theta} \right) + \dot{Q}_v''' = 0 \quad 4.6$$

This derivation will form the backbone for the numerical model used. The modelling of the internal heat generation will be discussed later in the chapter. Although equation 4.6 can be solved for a constant internal heat value, it will be proved later in the chapter that the internal heat is not constant.

### 4.3 Numerical Matlab model

The numerical models were built using a finite volume method. This method is especially handy when conduction problems need to be addressed. The first step in constructing a finite-difference solution procedure is to discretize the spatial coordinates to form a mesh of nodes. A differential equation is constructed next by applying an energy conservation principle directly to the control volume (as specified in Figure 24). In steady state heat conduction problems, a set of linear algebraic equations is obtained with as many unknowns as the amount of nodes there are in a mesh. This set of algebraic equations is then solved by an iterative method that will be explained later in the section.

There were two different MATLAB models developed, the first being an one-dimensional model, which only takes a temperature increase in the y-direction into consideration and neglects the conduction in the normal direction (x-direction). This one-dimensional model is very simple and the results can be compared to that of an analytical solution which will contribute to the validation of the two-dimensional model. This model will also be used to initialize some of the early modification in the two-dimensional problem to speed up the convergence rate.

In the case of irregular circumferential flux distribution, the heat transfer is multidimensional. A two-dimensional model was then developed from the one-dimensional analysis. Since both models are based on the same principal, a more in depth description will follow for the two-dimensional model, since it is more complicated.

Using the principle of conservation of energy requires that over a time interval ( $\Delta t$ ), the change in internal energy in the system is equal to the heat transferred into the system plus the heat generated within the system.

$$\Delta U = \dot{Q}\Delta t + \dot{Q}_v\Delta t \quad 4.7$$

By simplifying equation 4.7, assume steady state analysis and use compass direction (N, S, E and W) for the different faces leads to a two-dimensional steady state conduction model. The definition of the control volume and the direction can be seen in Figure 26 and Figure 27 respectively.

$$\dot{Q}_x|_W + \dot{Q}_y|_S - \dot{Q}_x|_E - \dot{Q}_y|_N + \Delta\dot{Q}_v = 0 \quad 4.8$$

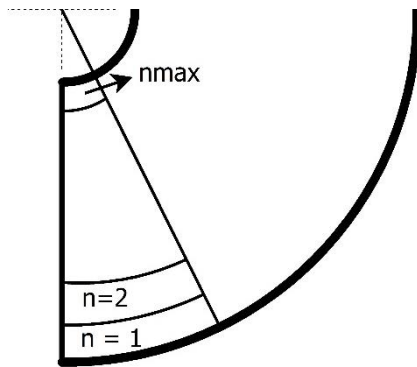


**Figure 26: Section of control volume**

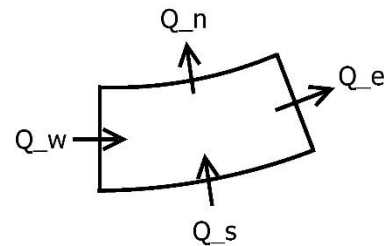


**Figure 27: Single control volume element**

In order to establish a node configuration, the 'n' nodes are numbered from South to North and the 'm' nodes are numbered in the circumferential direction, from West to East. This representation can be seen in Figure 28.

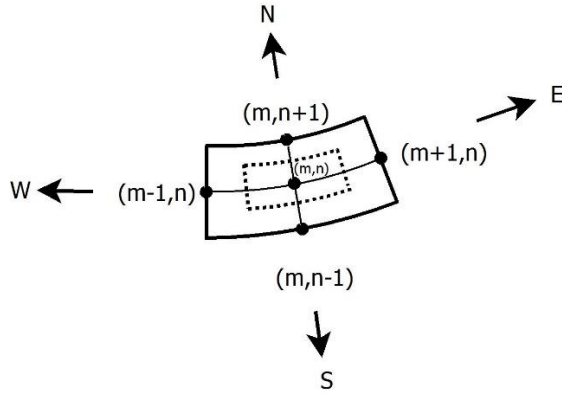


**Figure 28: Node numbering format**

### 4.3.1 General case

For the general case where the control volume is not subjected to any boundary conditions:

$$\begin{aligned}
 & -\frac{kA|_W(T_{m,n} - T_{m-1,n})}{dr} - \frac{kA|_S(T_{m,n} - T_{m,n-1})}{dr} \\
 & + \frac{kA|_E(T_{m+1,n} - T_{m,n})}{dr} + \frac{kA|_N(T_{m,n+1} - T_{m,n})}{dr} \\
 & + \dot{Q}_{v,in} - \dot{Q}_{v,out} = 0
 \end{aligned} \tag{4.9}$$

The areas,  $A|_W$ ,  $A|_S$ ,  $A|_E$  and  $A|_N$  refer to the cross section area over the face of the specific direction analysed.

$$A|_E = A|_N = drdz \tag{4.10}$$

$$A|_S = dz(r + dr)d\theta \tag{4.11}$$

$$A|_W = dz(r - dr)d\theta \tag{4.12}$$

The net internal heat generation term can be replaced by the solar flux entering the control volume minus the solar flux leaving the control volume. The internal energy term can be described as follows:

$$\dot{Q}_v''' = \left( \frac{\dot{Q}}{dxdydz} \right) = \frac{\dot{q}_{solarflux} A}{rd\theta dzdr} \tag{4.13}$$

Substituting the solar flux term by equation 2.11 and simplify the expression leads to:

$$\dot{Q}_v''' = \frac{I_o \exp(-\kappa\zeta)}{dr} \quad 4.14$$

Where  $\zeta$  is the length the solar ray had to travel through the porous medium to the specific point and  $I_o$  is the measured incoming DNI. When equation 4.14 is substituted in equation 4.6, it can be seen that the equation cannot be separated which suggests there is no analytical solution available. Not only will the numerical Matlab model replace the analytical solution, but it can also handle a non-uniform flux distribution.

### 4.3.2 Boundary conditions

Convection losses will dominate the losses in the outer tube of the receiver as the surface temperature is still relatively low for current test setup. Therefore will the outer boundary condition in the South direction be:

$$h_c A|_S (T_\infty - T_{m,n}) \quad 4.15$$

Since it is assumed that the inside temperature of the tube will be the same as the measured inlet air, the boundary condition on the outside of the copper pipe will be that of a constant temperature.

$$T_{m,n+1} = T_s @ constant T = T_{inlet air} \quad 4.16$$

The model will be modified to run as a symmetric model or a normal model, without symmetry, depending on the application. For symmetry the conduction over the West face of the control volume can be neglected, as can be seen in equation 4.17.

$$\frac{dT}{dr} = 0 \rightarrow \dot{Q}_W = 0 \quad 4.17$$

### 4.3.3 Formulation of critical constants and variables

The porosity is a measure of the void spaces present in a space partially filled with a material. The porosity of the copper wool was determined by weighing the amount of copper wool present in the system, while knowing the density of the material (brass). The total mass of the copper wool can then be divided by the density to get the volume of the amount of copper wool. The porosity of the configuration is then (Kaviany, 2012):

$$\varepsilon = 1 - \frac{V_{material}}{(V_{total})_{air}} = 0.98 \quad 4.18$$

As previously stated that the air and copper wool are modelled together with an effective thermal conductivity, it can be determined as followed (Aichmayer, 2011; Wu *et al.*, 2011; Nield & Bejan, 2013):

$$k_{eff} = \varepsilon k_{air} + (1 - \varepsilon)k_{medium}$$

with  $\varepsilon$  being the porosity determine by equation 4.18 and  $k_{medium}$  being the thermal conductivity of the copper wool which was assumed to be brass with a value of 110 W/m K (Çengel & Cimbala, 2009). The manufacturer specified it as brass, but could not supply the material properties.

#### 4.4 CFD analyses of receiver

The use of a CFD analysis will mainly focus on the heat penetration, the radiation effects and external forced convection in the receiver. The discussion will start by analysing the mesh of the model by moving on to the setup of the different conditions. This will include the boundary conditions, cell zone condition and also the material properties. The simulated CFD model brings two new elements to the table. The first being that convection is included in the simulation and the second is that a more “complete” radiation model can be used, which will include directional effects as well as emissions.

##### 4.4.1 Model design

The mesh was created with the standard ANSYS meshing software, by making use of sweepable body parts. The mesh created for the receiver can be seen in Figure 29, with the collector analyses neglected for this specific analysis, since modelling the collector and the specular reflection from it will be very resource intensive in the three-dimensional domain. To increase the computational speed, only a symmetric half of the receiver was modelled.

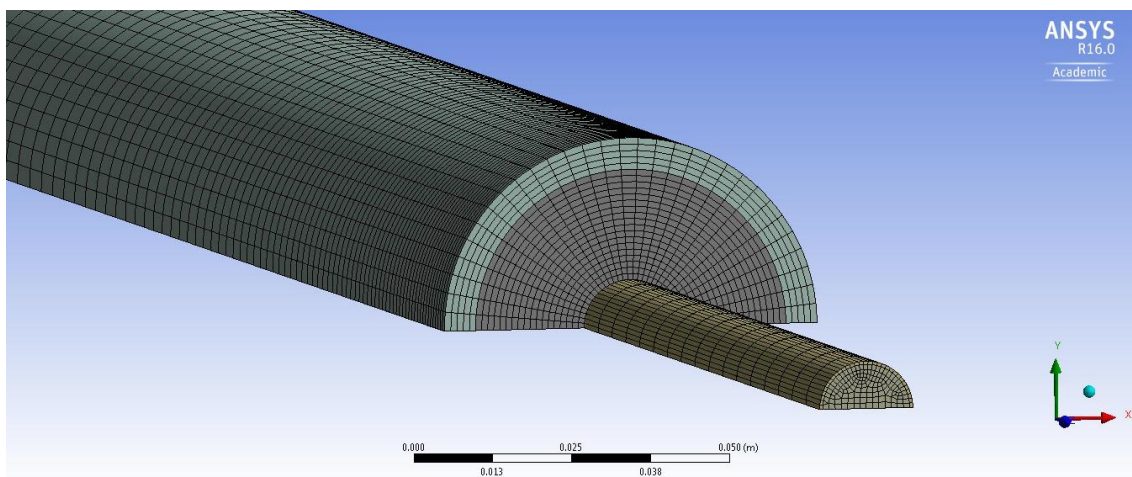


**Figure 29: Mesh profile of the receiver**

One of the features used by ANSYS to increase the quality of a mesh is edge and face sizing. This feature will determine the cell size according to the detail on the edge line. Where there are more detail, a finer mesh will be created and where the cells are not

near the wall, a more coarse mesh will be generated. This will not only increase the quality of the mesh, but will also increase the solution time. These features can be seen in Figure 30 below where the image on the left shows the edge sizing and the image on the right the face sizing.

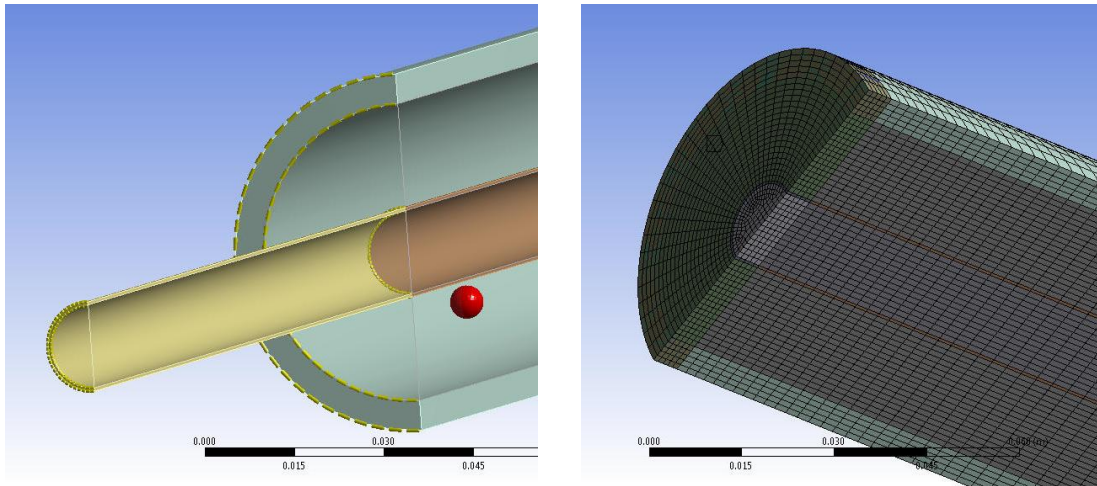


**Figure 30: Edge sizing and face sizing**

The mesh was checked and cleared for any bad quality cell. The maximum aspect ratio on a cell was 47, the maximum orthogonal skewness was 0.21 and the minimum orthogonal quality was 0.78. An ideal mesh will have an orthogonal skewness of zero and an orthogonal quality of one. The mesh consist out of 182 795 elements, which are predominant quad cells.

#### 4.4.2 Model setup

The mesh that was created from the model was imported to Fluent, a general purpose commercial and academic CFD code, used to model the physical properties of the system in order to do various analyses. This is an extremely powerful tool that can be used, but in the same sense, very misleading if not handled properly.

In order to model the flow in the receiver as closely to the experimental setup as possible, conservation of mass, momentum and energy have to be solved in order to determine the fluid behaviour.

The Discrete Ordinates Radiation model will be used to simulate the radiation of the solar flux by defying semi-transparent walls at the boundary of the source field which solves the radiation transfer equation as given by equation 2.13. The model divides a plane or target in a finite number of solid angles, each associated with a specific vector direction that is fixed to the global co-ordinate system of this study (x, y, and z).

The non-gray model is used to divide the wavelengths into two different interval bands, one for wavelengths smaller than  $2\mu\text{m}$  and the other interval for wavelengths between  $2\text{-}100\mu\text{m}$ . This will allow for the large wavelengths to be absorbed in the glass and the short wavelengths to penetrate through the glass.

The angular discretization takes place in each octant of the  $4\pi$  angular space with  $N_\theta \times N_\phi$  solid angles. By dividing the plane of radiation into sections and assigning properties to the cells within the target, a concentrated solar flux can be simulated. Each of the directions that pass through more than one control volume (called overhanging control angles) are divided into  $N_{\theta,p} \times N_{\phi,p}$  pixels. The energy in each of the pixels is then treated as incoming or outgoing to the face. The pixels were set to  $3 \times 3$  pixels for every solid angle (ANSYS Inc, 2013).

To model the airflow in the receiver the standard two equation turbulence model will be used due to the many disturbances in the flow which occurs in turbulent flow regimes. The k- $\epsilon$  model will be best suited for the experimental setup since it is robust, accurate and computationally inexpensive to use (ANSYS Inc, 2013,p.47).

The model will use a Simple Pressure-Velocity Coupling scheme with a least square gradient since the solution is assumed to vary linearly. This model will also be chosen for its robustness to model different flows.

#### **4.4.3 Material specification**

The air fluid inside the copper tube will have the same properties as the air passing through the porous medium, except that a porosity constant is assigned to the flow through the annulus. It will be assumed that the air will have constant properties throughout the whole flow process.

The porous medium that is used consists of a brass material which is a compound of copper (70 %) and zinc (30 %). The density of the brass is specified as  $8530 \text{ kg/m}^3$  with a specific heat constant of  $380 \text{ J/kg K}$  and a thermal conductivity of  $110 \text{ W/m K}$  (Çengel & Ghajar, 2011). The fluent material data base will be used to assign the properties of the pure copper pipe transporting the inlet air.

The quartz tube will be assigned to the band specified previously in the chapter that absorbs all the long wave radiation. The material has the following constant properties: density of  $2230 \text{ kg/m}^3$ , specific heat constant of  $871 \text{ J/kg K}$  and thermal conductivity of  $1.14 \text{ W/m K}$ .

The rubber that will be used as the air stop is normal commercial rubber with a density of  $1100 \text{ kg/m}^3$ , a specific heat constant of  $1680 \text{ J/kg K}$  and a thermal conductivity of  $0.032 \text{ W/m K}$ .

#### **4.4.4 Cell zone conditions**

The cell zones were divided into five different parts: the inlet air flowing through the copper pipe, the air where it changes direction, the porous medium, the copper pipe itself and lastly the glass tube.

The air that enters the system through the copper pipe will not be affected by radiation, which means that heat transfer will only be by heat conduction. This assumption will speed up the computation and is valid since the copper pipe is opaque. Once the air leaves the copper pipe, it will gain energy through convection and radiation.

The porous medium will be constructed with the air as the porous zone. This air will be assigned as the fluid material and the brass will be the solid material. The porosity, as determined in section 4.3.3, was specified here to be 0.98. Fluent uses this value to determine the effective thermal conductivity of the porous zone, as also described in section 4.3.3 (ANSYS Inc, 2013).

The radiation is treated as a local thermal equilibrium (LTE) model which means that the temperature of the fluid (air) is the same as the solid temperature (porous medium). Due to the high heat transfer coefficient and large heat transfer surface between wires and air, the LTE model is valid (Wu *et al.*, 2011; Mahmoudi & Karimi, 2014). The scattering is also modelled as independent scattering which means that the medium and the specific particle is not influenced by the scattering of the neighbouring particles, therefore the attenuation coefficient can be separated into absorption and scattering. Thus by assuming that the particle gain exactly as much from in-scattering as it loses through out-scattering, the absorption is only modelled (Baillis & Sacadura, 2000).

The copper pipe will not participate in radiation, as it is opaque and will only have surface effect. As discussed in equation 2.12, this value will be dependent on the absorption coefficient. The glass tube on the other hand will absorb about 8 % of the irradiation from the collector, as discussed previously, and will definitely participate in the radiation energy equation since it is semi-transparent.

#### 4.4.5 Boundary conditions

The specification of the boundary conditions is the most important part of the setup, since it contains a lot of detail and assumptions. The inlet and outlet will first be discussed followed by all the wall conditions with all the assumptions.

The inlet air temperature was set at the average measured temperature, which differs from the different test sets, varying from 304 – 306 K for each set. For the steady state testing and modelling purposes, the mass flow and pressure was kept constant at 123 l/min and 0.5 bar which gives an inlet air speed of 13.3 m/s and gauge pressure of 50 000 Pa. The outlet end is open to the atmosphere, which mean that a zero gauge pressure is present at the outlet.

The glass tube was modelled as a semi-transparent material with a constant surface flux value. The DNI reading for each experimental sets differs which mean that the Direct Irradiation constant will also be varied between 6000 and 6200 W/m<sup>2</sup> in the radiation model (when each of the different test were analysed). Note that this value will only be assigned to the short wavelength band, and a zero value for the long wave band. The beams will be coming in parallel with regards to each other, in the negative y direction vector. This simulation of parallel beams will be used since it is computationally cheaper and it will allow consistence in the numerical Matlab model as well as the simulated CFD model.

The porous medium does not have any major influence on the boundary conditions, since it is only converting the energy. The constant that will be changed is the emissivity which is 0.15 for weathered surface brass (Çengel and Ghajar, 2011,p. 889).

The copper pipe will absorb and reflect some of the radiation that penetrated through the whole thickness of porous medium. The emissivity is thus set to 0.15, which is valid

for commercial copper (Çengel and Ghajar, 2011, p. 889). The other wall boundary conditions that have to be specified, is that of the rubber at the end of the tube, where the airflow changes direction. The rubber will have an emissivity of 0.9 (Çengel and Ghajar, 2011, p. 889)

Due to a symmetrical configuration, only a 180° domain have to be simulated. This will decrease the computational time and will be much cheaper to simulate in terms of computational costs.

#### 4.4.6 Data to be collected

The simulated data will be gathered by means of different type of simulations. The first simulation will be to determine the solar fluxes on the receiver. This will display a concentrated solar distribution around the glass tube. This information will identify critical zones where hotspots may occur.

The most important part of the simulation is to gather the data of the temperature distribution in the radial direction at different sections. This data will then be compared to the numerical Matlab model data as well as the experimental data. The receiver will then be analysis for any defects or hotspots.

#### 4.5 CFD description of the two-dimensional radiation model

The radiation model aims to determine the concentrated solar flux on the outer tube. A two-dimensional domain was created where the parallel incoming rays is reflected from the mirrors to the receiver situated above the collector. This will give an indication whether or not a uniform flux can be used in the analyses.

The mirrors were specified to have a reflectivity of 0.82 as given by the manufacturer. The incoming flux was specified as the same value as the DNI readings from Sonbesie, during the testing period. The result of this model will be discussed later in section 5.3.

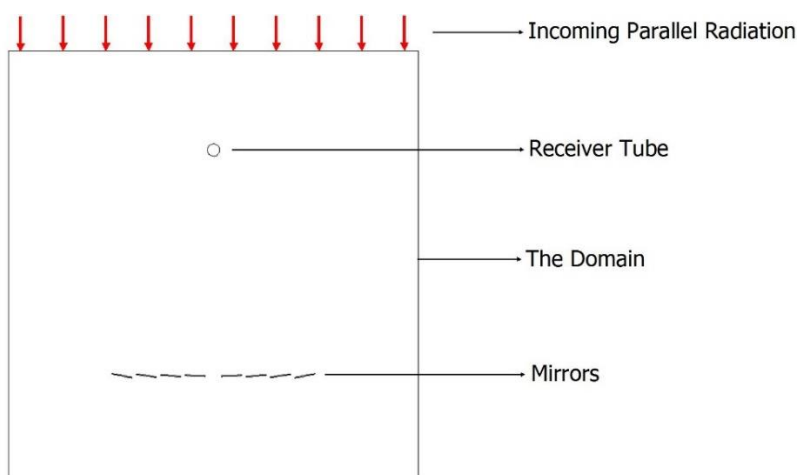


**Figure 31: Radiation model setup**

## CHAPTER 5. RESULTS AND ANALYSES

One of the objectives of the study is to determine the feasibility of the air receiver, by means of determining the efficiency of the system. The higher the temperature difference between the inlet – and outlet air, the higher will the efficiency be. Since there are no similar studies in the field of air receivers, the system will be validated by means of the simulated CFD model. The numerical Matlab model will be another mechanism that will be used to compare the results between the simulation model and experimental results.

### 5.1 Experimental results

The experimental test were done during different months, it was started in March 2015 and ended in April of the same year. These tests ranged over different weather conditions, which included a blistering 43 °C day with a measured DNI rating of 973 W/m<sup>2</sup>. The different conditions, including the wind speed, irradiation and atmospheric temperature, were taken into account for each test to increase the credibility of the results and efficiency calculations. Sonbesie weather station is situated on top of the Civil Engineering building where accurate weather readings can be taken, which is not the case with the experimental setup. The setup is placed between buildings which create disturbances in terms of wind speed and direction. Although the data is not exactly the same at the different locations, it is the best available source of information.

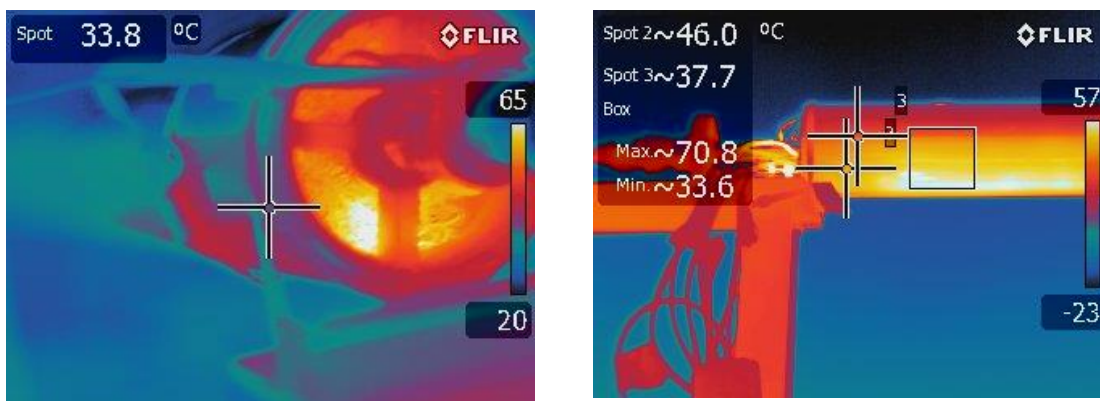


**Figure 32: Thermal imaging of the receiver**

The photos in Figure 32 were taken with The FLIR camera that can capture the surface temperature by using infra-red signals. The image on the left shows the hot spots in the absorber material. It is clearly visible that the highest temperature is present at the bottom of the copper wool, where the irradiation is concentrated. What is surprising, however, is that the temperature of the absorbing material and the air at the outlet is almost the same. Although this was assumed in the numerical and simulated model, for simplicity purposes, it was not expected. This unexpected result might be due to the uneven surface of the copper wool that can give inaccurate surface temperature readings by the camera. This procedure was repeated that led to the same result.

The picture on the right in Figure 32 shows the surface temperature of the quartz tube. These temperatures were calibrated by using a single thermocouple at different points on the tube, which is available in APPENDIX C. The surface temperature of the receiver tube will be used to calculate the radiation losses from the receiver to the sky. This value will be relatively small for low surface temperature, but is significantly large for high surface temperature, which can be seen in equation 2.30.

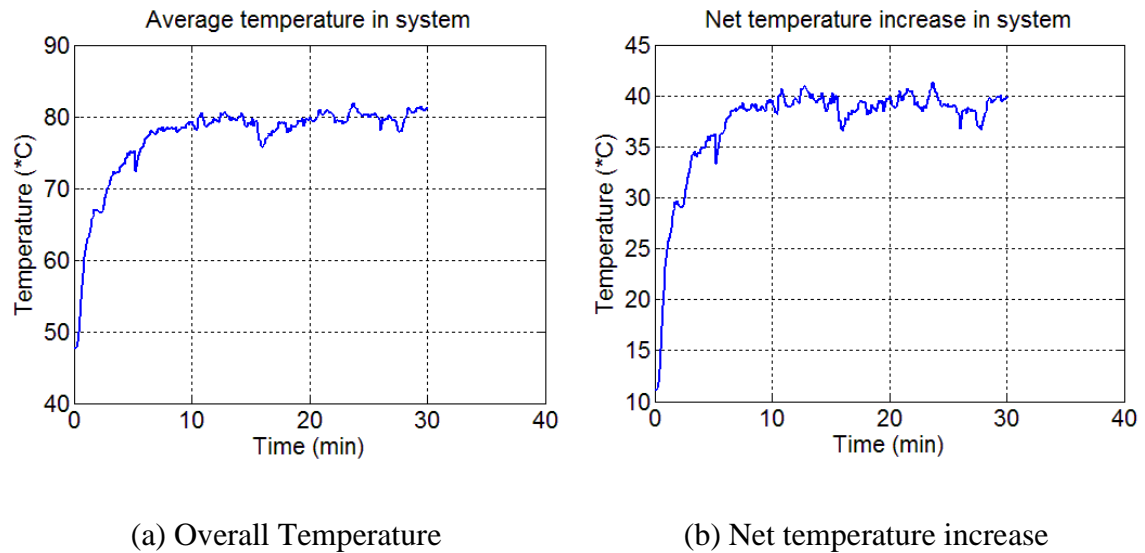


**Figure 33: Measure temperature in test 1**

Different tests were conducted during the testing period. The first test took place on the 30<sup>th</sup> of March 2015 at 11:55 am, with a maximum ambient temperature of 43 °C and DNI of 973 W/m<sup>2</sup>. The data of the first test can be seen in Figure 33, with the average temperature over the whole radial distance on the left and the average temperature increase in the system, on the right.

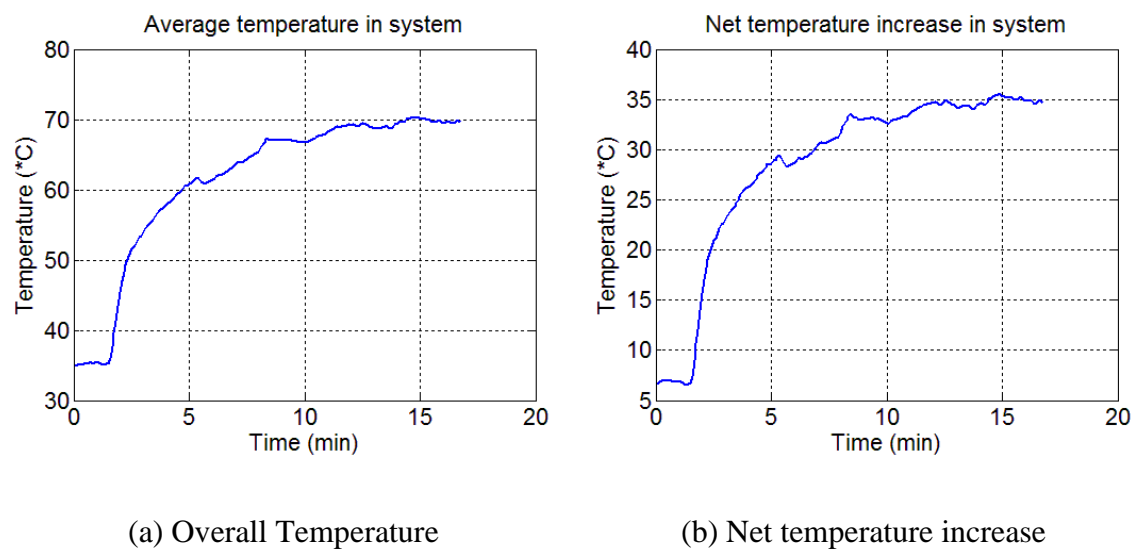


**Figure 34: Measure temperature in test 2**

The test in Figure 34 was done on the 24<sup>th</sup> of April 2015 at 11:15 am, with a maximum ambient temperature of 28 °C and a maximum DNI of 963 W/m<sup>2</sup>. The data is smoother since the tracking was adjusted more often, instead of every 3<sup>rd</sup> minute it was changed to every 2<sup>nd</sup> minute. It is clearly visible that the net temperature increase in the system was higher during test 1, which was done on a day with a higher DNI value.

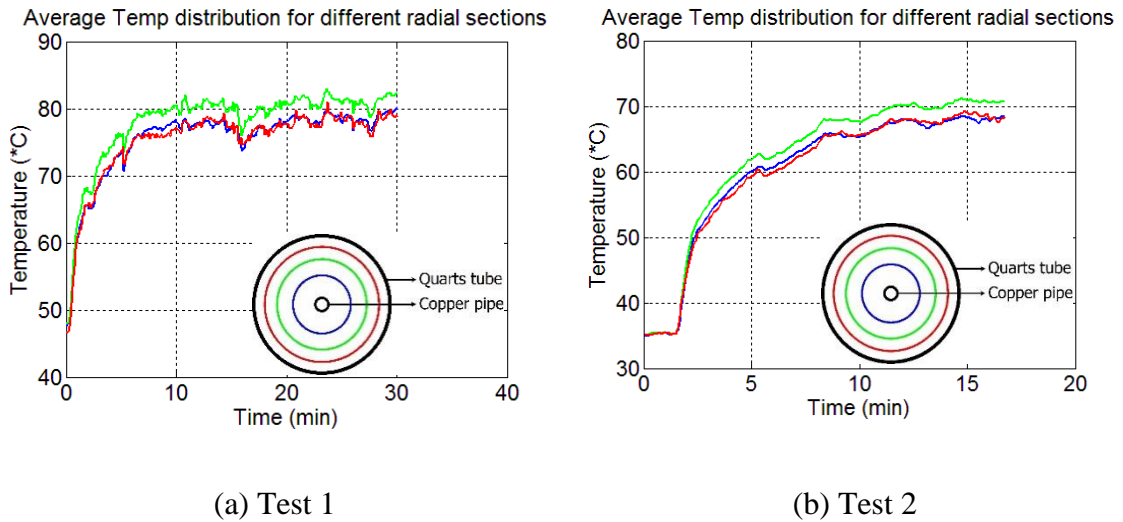


**Figure 35: Temperature distribution for different tests**

When the average temperatures for the different radial distances are compared in Figure 35, it is evident that the highest temperatures is at the mean radial distance from the centre of the copper tube. The temperatures closer to the quartz tube and the copper pipe are generally the same, but differ from time-to-time. This means that the temperature profile in the receiver tube is a parabolic one, peaking towards the middle of the annulus.

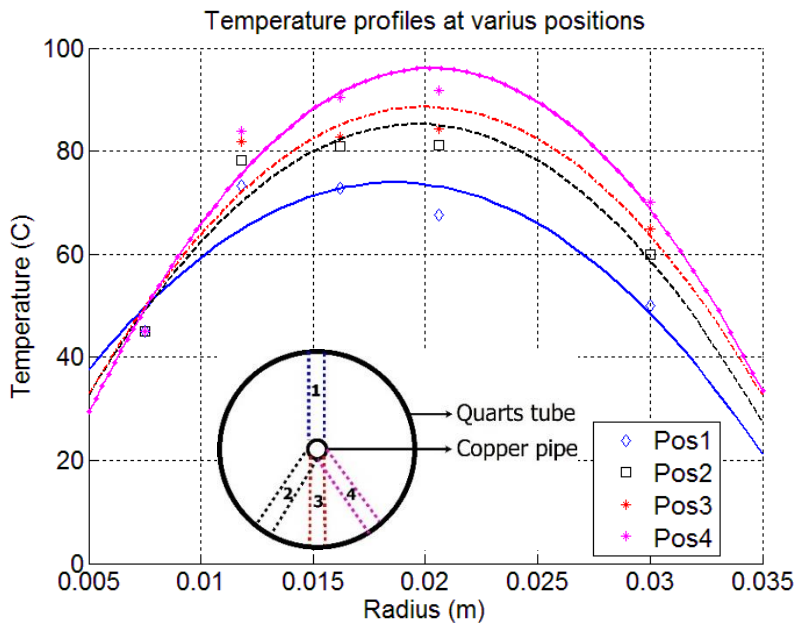


**Figure 36: Temperature profile for different sections**

The different temperature profiles within the receiver can be seen in Figure 36. Note that the colour schemes in the legend match that of the graph. It follows that the highest temperature is present at position 4, which is expected since the highest flux will be normal to the rays, as explained in Figure 23, of the different coordinate system. It can be seen that a parabolic temperature profile is always present at all the outlet sections considered. These experimental results will be compared, later in the chapter, to the results of the simulated CFD model as well as the numerical Matlab model.

## 5.2 Numerical Matlab model results

The main purpose of the numerical model was to determine whether the scattering coefficient can be neglected, by assuming that the radiation attenuation is a function of the absorption coefficient only, as stated in equation 2.11. These results can be seen in Figure 37 below.

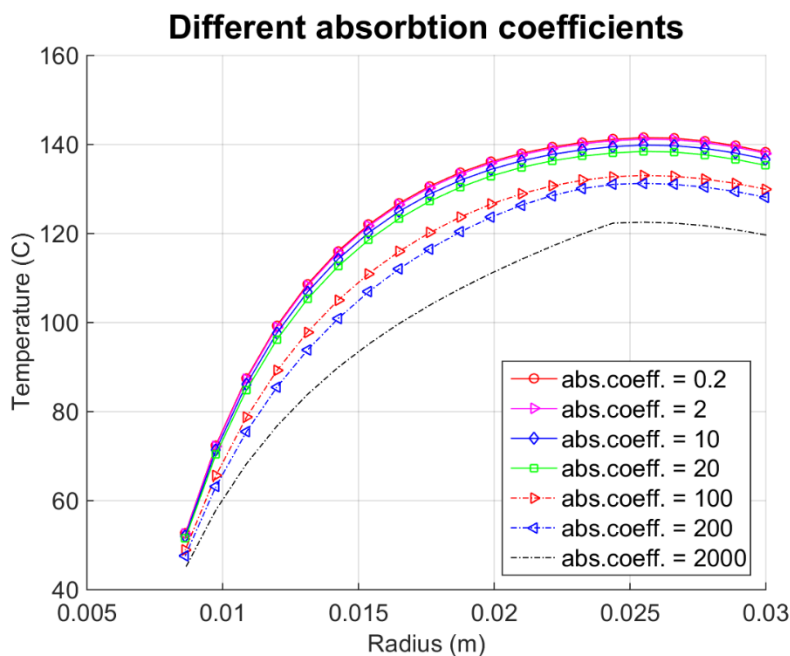


**Figure 37: Evaluating different absorption coefficients**

According to the numerical results, temperature at the outlet will only decrease as the absorption coefficient increases. It was expected that the peak temperature will shift in the radial direction, towards the quartz tube side, while the maximum temperature staying relatively constant, however, that is not what the model predicts. It follows that the different profiles cannot be linearized and compared to the experimental data to determine the exact absorption coefficient, as the initial problem definition statement.

This concludes that the absorption coefficient cannot be determined from the numerical Matlab model itself and will need to be determined through experimental work that consists of a separate test setup to that of the receiver.

### 5.3 Simulation results

The first simulated CFD model was developed to establish a temperature profile on the receiver tube. The results can be seen in Figure 38 and Figure 39 below. It is important to have a constant radiation flux profile when the different models are compared.

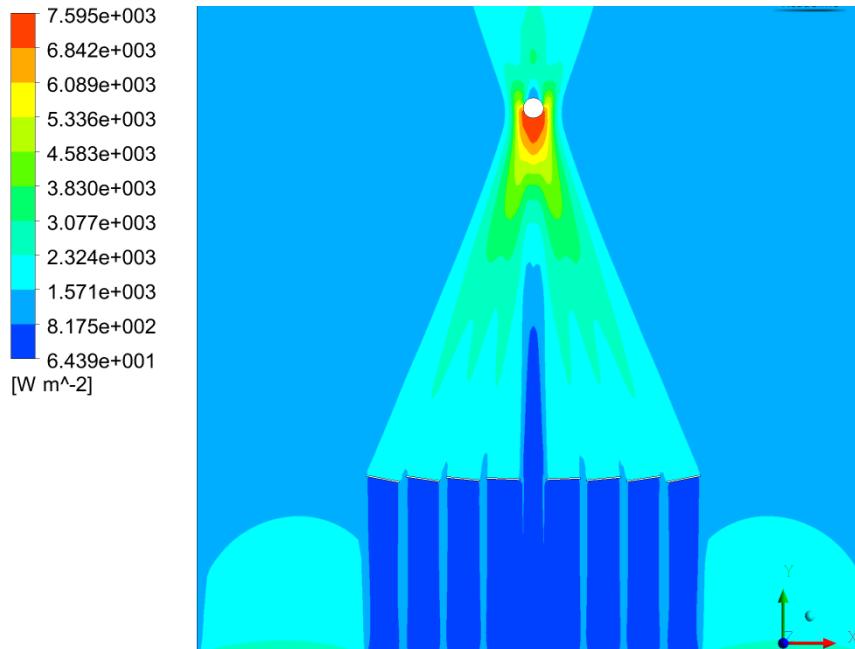


Figure 38: Radiation flux distribution

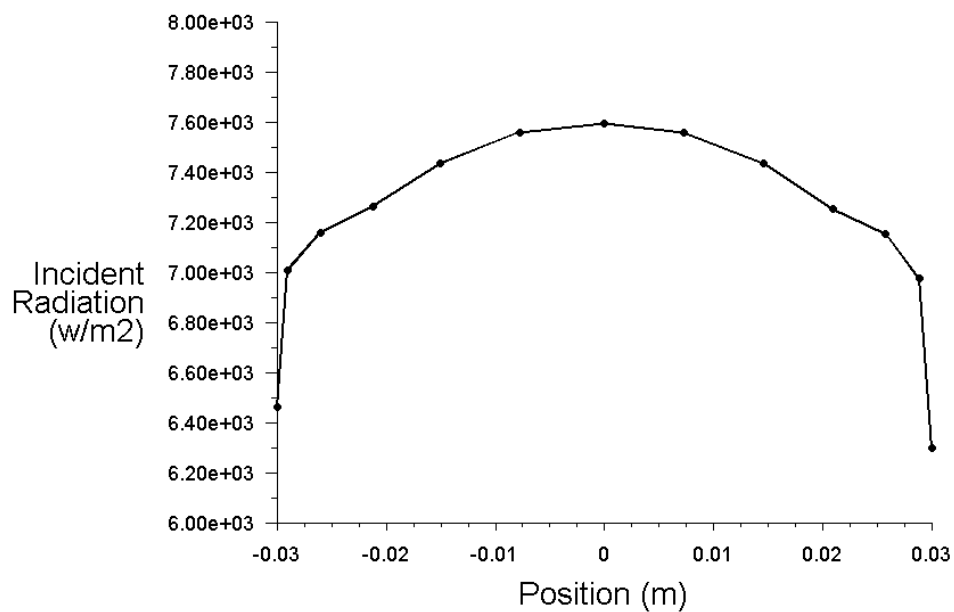
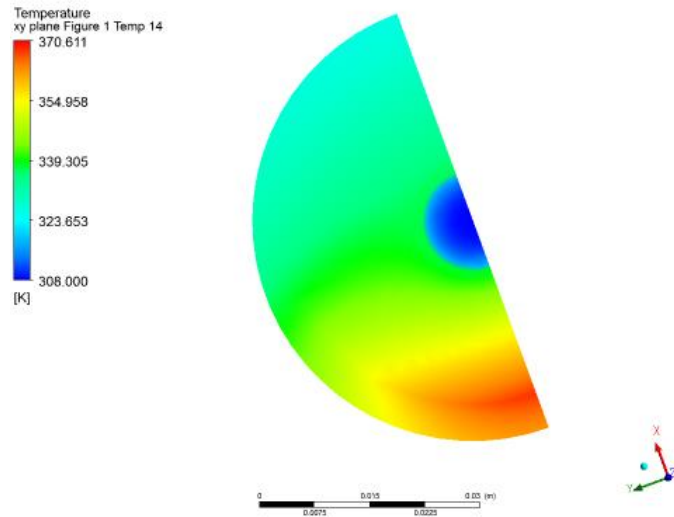


Figure 39: Simulated radiation profile

It is clear that the radiation model used to determine the radiation profile works well and give good and accurate results, compared to the measured solar flux. The radiation distribution is also constant at the bottom half of the tube, as can be seen from Figure 39. The experimental results cannot be plotted in the same manner, but the average concentrated radiation is  $6524 \text{ W/m}^2$  (as calculated in APPENDIX C).



**Figure 40: Temperature distribution at outlet**

When the focus is placed on the temperature inside of the tube receiver, it can be seen that there is a large temperature difference between the bottom and the top part of the tube. This symmetrical temperature profile at the outlet of the tube is displayed in Figure 40. The image is rotated anti-clockwise to be in the  $x_1, y_1$  coordinate system (as defined in Figure 23), which will simulate the experimental setup. This temperature distribution compare well with the results of the FLIR camera (Figure 32), although the simulation assume the air and porous medium to be of the same temperature.

This image can also be used to get the temperature profile for different sections in the tube. The specific focus was placed on the area parallel with the rays, vertically on the  $y_1$  axis, where the highest flux will be present.

The temperature profiles at different parts of the receiver are studied in Figure 41 and Figure 42 respectably. The first image analysis the flow at the outlet, whereas the second one is taken halfway through the tube, lengthwise.

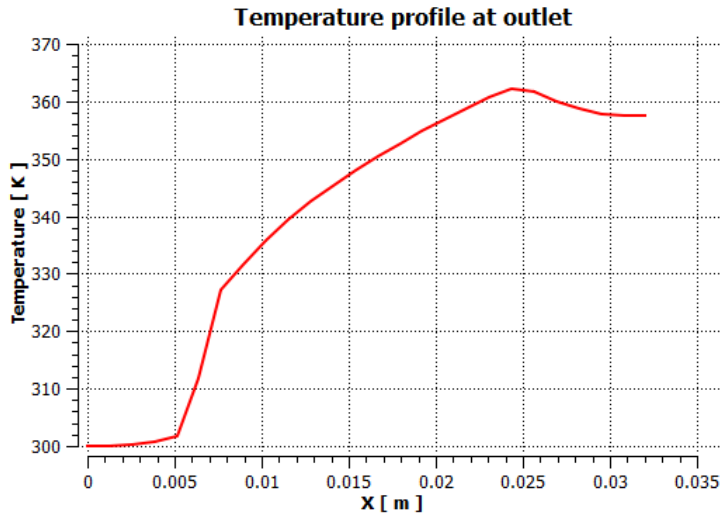


**Figure 41: Temperature profile at the outlet**

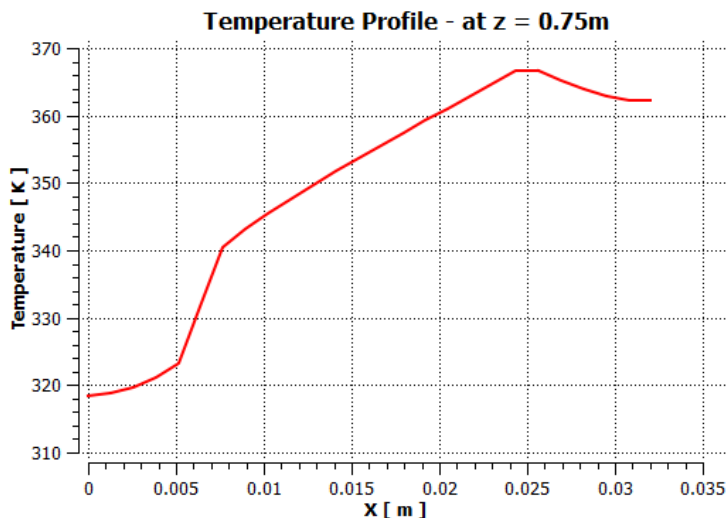


**Figure 42: Temperature profile halfway through the tube**

The temperature is lower at the outlet, than at the middle of the tube. This is due to external environmental effects, like the back pressure temperature, which was assumed as the ambient temperature during testing and also mixture with ambient air. This will, however, not be the case if the air was to be expanded through a turbine, instead of releasing it to the environment.

The results of Figure 41 will be compared to the experimental result in Figure 36, as well as the numerical Matlab model which only looked at the radiation aspects of the system. This comparison will look to validate the experimental results with the simulated results.

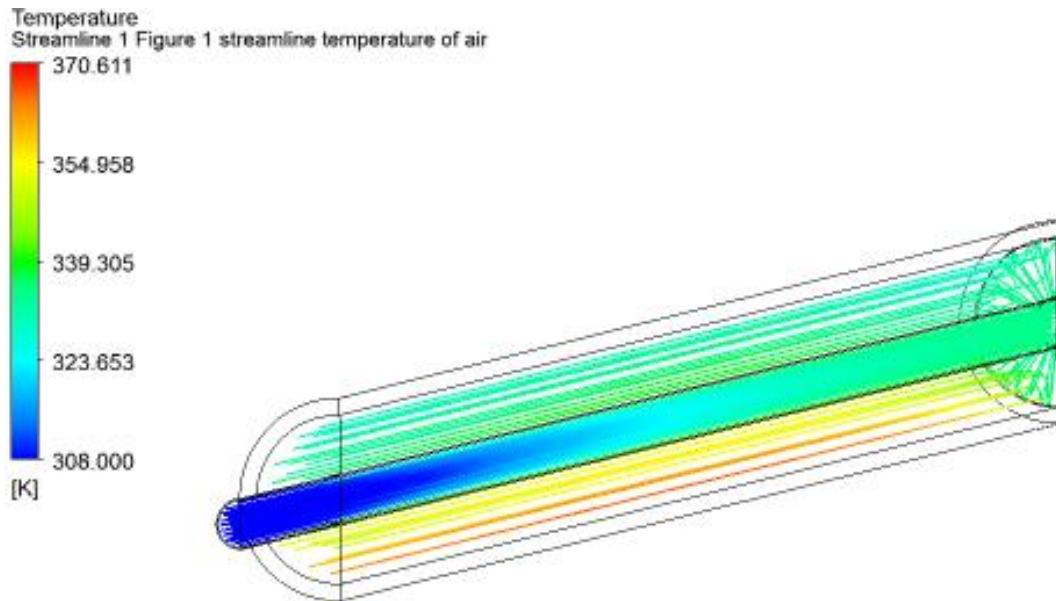


**Figure 43: Streamline temperature of the air**

The particle streamline function was used in ANSYS to trace the air temperature within the system, which can be seen in Figure 43. It is clear that the temperature of the air increases as it passes through the inside of the copper pipe, and not only in the porous medium. The largest temperature increase is, however, at the bottom of the receiver tube, where it is subjected to the highest flux.

#### **5.4 Combined results and analyses**

Due to the lack of research in this field of receivers, the only form of comparison can be done by own experimental and simulated work. This section will aim towards validating the experimental work as well as the simulated CFD models.

The first comparison can be seen in Figure 44, which compares the simulated result to that of the experimental results. The data was compared at the highest flux region, which is on the vertical line of the  $y_1$  axis. To illustrate this, the setup of Figure 40 was compared to the result of position 4, in Figure 36.

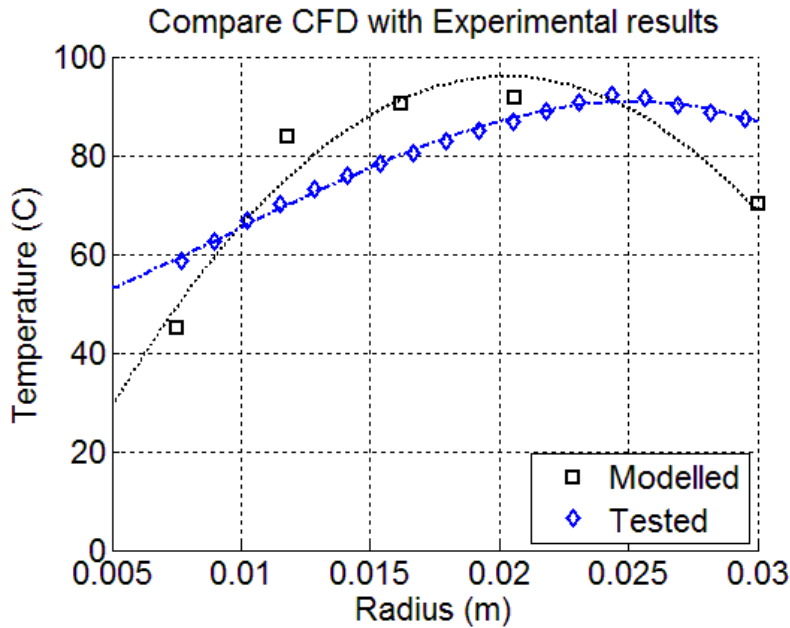


**Figure 44: CFD model compared with experimental data**

The results show a good correlation between the experimental and simulated results in CFD. There is a slight difference in the results, but the simulated model can't take all the external losses into consideration, which were done to simplify the model. The assumption that all the radiation gets absorbed in the porous medium, which mean that the temperature of the inside and outside of copper tube, is the same, might not be that valid. However, the limiting space in the tube constrained the total amount of measurements that could have been taken on the same radial line.

The next comparison will be done between the numerical Matlab model and the simulated model. Since the numerical model also took radiation into consideration and no convection, the models cannot be compared directly. However, the temperature profiles can be compared with each other, which has been done in Figure 45.

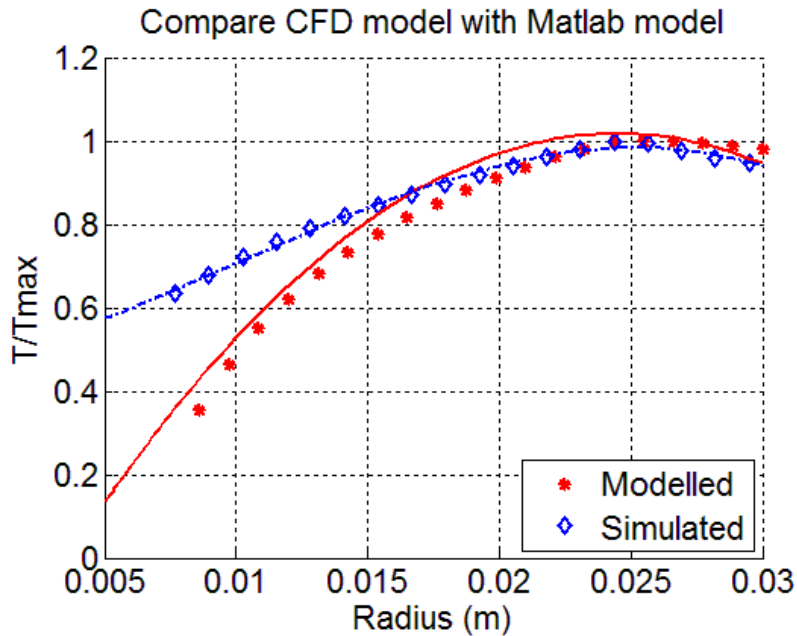


**Figure 45: Linearized comparison of temperature profiles**

There is a very good relationship between the two models, especially close to the glass wall ( $0.015 < r < 0.03$ ), where the radiation is at its highest. However, as the radiation concentration decreases, the models react differently to the variations. This means that the simulated model is less dependent on the radiation due to convection losses.

### 5.5 Overall efficiency of receiver

The overall efficiency of the receiver was determined to be 41 % with the major part of the losses being that of convection to the atmosphere. This value cannot be compared to other receivers, since the optimization of the receiver tube is not within the scope of the project.

The average measured wind speed over the testing period was 4 m/s and was assumed to be always normal to the tube. This is a conservative assumption and will have the highest losses possible. The spillage from the mirrors was neglected in the calculation, since the receiver tube efficiency was calculated and not the collector itself. The receiver losses breakdown is as follows: 79 % of the losses are due to convection and the other 21 % is due to radiation losses. The spillage was caused due to the over design of the mirror sizes. This had to be done to ensure that the collector is not sensitive to small changes.

## 5.6 Pressure losses in the tube receiver

The pressure loss in the system was also seen as an important aspect of the receiver design. Since the performance of the Brayton cycle is not only a function of temperature, but of pressure as well, the receiver aim towards having the smallest possible pressure drop (as stated in Chapter 2). The pressure loss in the receiver tube can be seen in Figure 46 below.

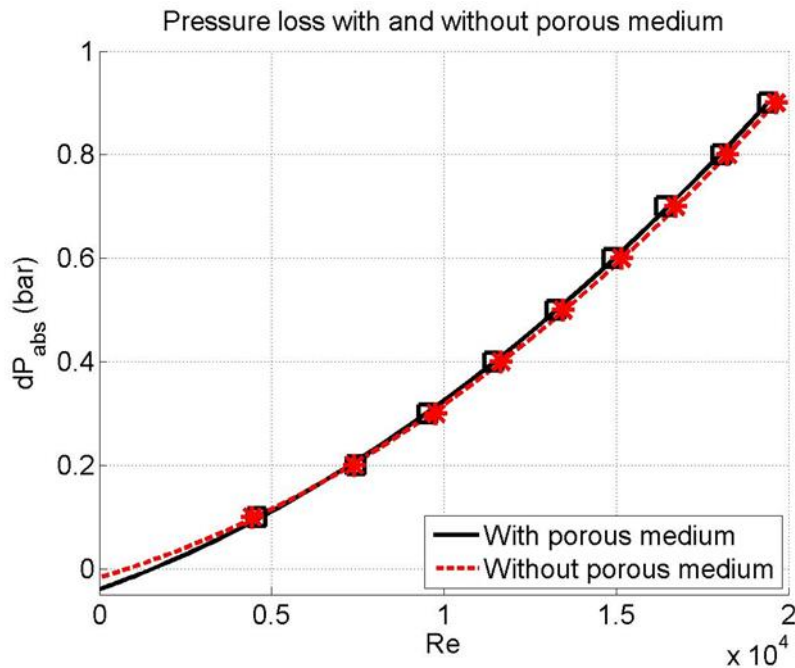


**Figure 46: Pressure losses with and without porous medium**

There is not a significant pressure drop caused by the porous medium, compared to the other pressure losses. This result is due to the high porosity of the air / porous medium ratio.

## 5.7 Verification of models

The most important aspect of the numerical Matlab simulation is to capture the physics in the model. In order to check whether the physics were “translated” correctly into the numerical model, a convergence check needs to be done. This will be done by doing an analysis to check if the model is grid independent. Not only do you have more accurate result, but doing this analysis will increase the computational speed of the model as well. Both models, numerical and simulated models were tested with regard to the grid size in Figure 47 and Figure 48 respectively.

The grid variation in the numerical Matlab model depends on the amount of nodes in the radial direction. Figure 47 shows the variation for the total number of nodes in the radial direction for each calculation. The model was programmed to change the tangential length of the elements according to radial length of the element. This will ensure that the aspect ratio of the element will not be out of proportion. In order to

determine the convergence in the model, the temperature profiles in the radial direction were plotted.

It is clear that the numerical results obtained from the Matlab model does not change a lot when the amount of linear nodes are increased to more than 20, as can be seen from Figure 47. This will only increase the computational cost with no increase in result. The ideal nodes size of 20 nodes, were used for all of the calculations.

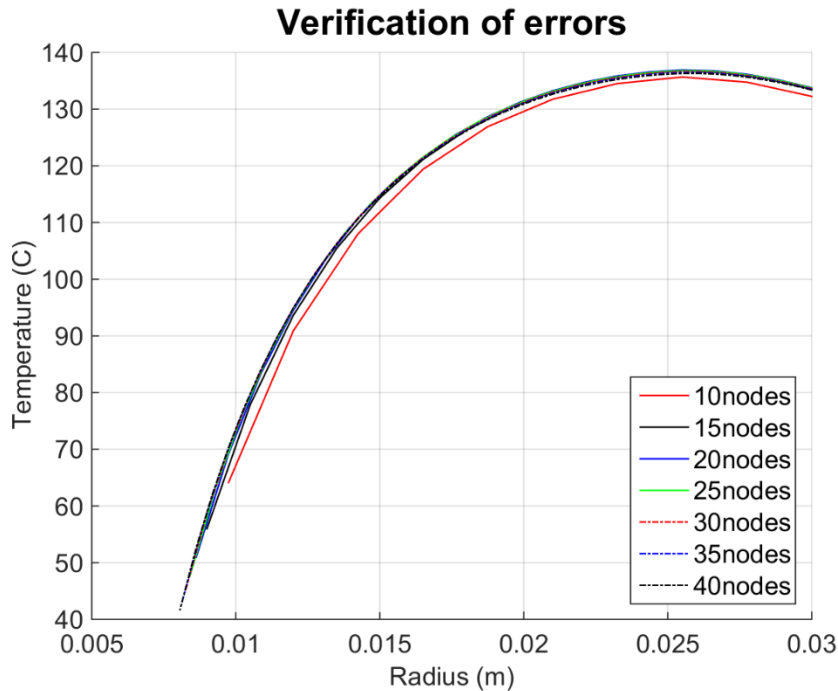


**Figure 47: Grid independence test of numerical model**

The simulated model in FLUENT uses advanced meshing techniques which increase the flexibility in the meshing procedure. For the above mentioned reason, the different mesh types were categorized in coarse, medium, fine and super fine meshes. The amount of nodes and elements for each mesh type can be seen in Table 3. The super fine mesh has almost eight times more elements than the coarse mesh and virtually 30 times the amount of nodes.

**Table 3: Mesh structures of the simulated model**

Mesh Structure	Elements
Coarse	30 300
Medium	93 345
Fine	181 463
Super fine	201 415

The temperature profile in the radial direction is again plotted in Figure 48 for the different meshing configurations.

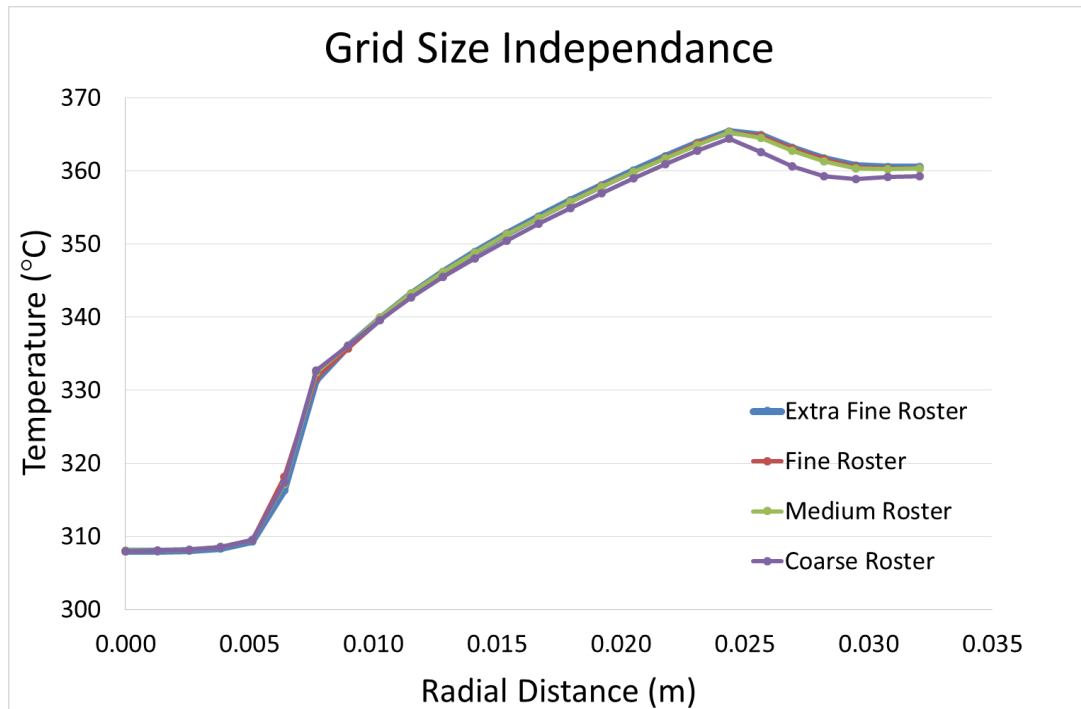


**Figure 48: Verification of different mesh types in simulated model**

It is clear from Figure 48 that the model starts to be grid independent from a medium size roster which have  $\pm 93\ 000$  elements. The medium roster could have been used, but for safety measures (in terms of inaccurate results), the fine roster was chosen to do all of the analyses. This will ensure that all the results are of high quality, without being too computationally expensive.

## CHAPTER 6. CONCLUSIONS

The main focus of the study was to develop an experimental test setup to evaluate the radiative properties of the porous medium, by taking temperature readings at different sections in the tubular receiver. Two different models were constructed, one simulation model in ANSYS and the other being a numerical model in MATLAB. The main goal of the simulated model was to mimic the experimental setup and to extract radiation data (extinction/absorption coefficient) from the experimental results. On the other hand, the numerical model was developed to determine whether the scattering coefficient can be neglected and if the absorption coefficient can be determined from the model.

The results from the experiment prove very promising. Without optimizing the receiver or the system, the receiver achieved a 41 % efficiency with an average temperature increase of up to 40 °C, while temperatures in excess of 100 °C were measured in parts of the system. The success of the system can be compared to a previous study done on the receiver, where an indoor setup was used and a temperature increase of only 9.6 °C could have been achieved (Hoffmann & Van der Merwe, 2014). The structure of the porous medium showed some vulnerability during the testing process. A separate test was done without any air flow through the pipe, which resulted in a colour change of the material due to the high radiation intensity from the collector. This was due to a bad quality material, which can be avoided in the future.

The simulated CFD model showed very promising results, as can be seen from Figure 44. Although the peaks of the temperature profiles do not occur on the same radial distance from the centre, the dominant parabolic shape profiles can be seen. These small deviations are due to external effect that cannot be modelled accurately and due to the assumptions that simplifies the model.

The assumption that the material and the air is at the same temperature will definitely have to be examined in future research on the project. This will, however, lead to very complicated simulations which might give inaccurate data. Once the temperature of the porous medium can be determined, the ideal material can be developed to handle the specific temperature, while maintaining great heat transfer capabilities.

The numerical Matlab model, on the other hand, showed good potential in verifying the simulated CFD model, but could not be used to compare it with the experimental results due to the complexity of modelling radiation and convection in porous medium. The numerical model showed that the scattering in the porous medium can be neglected, but the exact value of the absorption coefficient could not be determined from the model. When the temperatures were linearized in the two models, there was a clear relationship between the temperature profiles but no conclusive data to establish the absorption coefficient.

This receiver tube concept is promising when looking at the future of air receivers, but it has its limitations in with regards to material properties. A separate study will have to be conducted to determine the absorption and scattering properties of the porous medium. This will have to be done in a laboratory environment where external effects can be limited or in very high detailed CFD modelling where the wires are modelled individually. The main limitation of the concept lies in the material properties of the

porous medium. Although the porous medium showed some promising signs of high, non-optimized efficiencies, a material that can handle very high fluxes will be needed.

**REFERENCES**

- Aichmayer, L. 2011. Solar Receiver Design and Verification for Small Scale Polygeneration Unit. Royal Institute of Technology.
- ANSYS Inc. 2013. ANSYS Fluent Theory Guide.
- Ávila-Marín, A.L. 2011. Volumetric receivers in solar thermal power plants with central receiver system technology: A review. *Solar Energy*. 85(5):891–910.
- Baillis, D. & Sacadura, J.-F. 2000. Thermal radiation properties of dispersed media: theoretical prediction and experimental characterization. *Journal of Quantitative Spectroscopy and Radiative Transfer*. 67(5):327–363.
- Behar, O., Khellaf, A. & Mohammadi, K. 2013. A review of studies on central receiver solar thermal power plants. *Renewable and Sustainable Energy Reviews*. 23:12–39.
- Çengel, Y.A. & Cimbala, J.M. 2009. *Fluid Mechanics Fundamentals and Applications*.
- Çengel, Y.A. & Ghajar, A.J. 2011. *Heat and Mass Transfer: Fundamentals and Applications*.
- Copper Tubing Africa. 2015. Plumbing Code of Practice. [Online], Available: <http://www.coppertubing.co.za/> [2015, August 11].
- Craig, K.J., Gauché, P. & Kretzschmar, H. 2014. CFD Analysis of Solar Tower Hybrid Pressurized Air Receiver ( HPAR ) using a Dual-Banded Radiation Model.
- Department of Energy. 2013. Integrated Resource Plan for electricity 2010-2030.
- Fend, T. 2010. High porosity materials as volumetric receivers for solar energetics. *Optica Applicata*. XL(2).
- Fend, T., Hoffschmidt, B., Pitz-Paal, R., Reutter, O. & Rietbrock, P. 2004. Porous materials as open volumetric solar receivers: Experimental determination of thermophysical and heat transfer properties. *Energy*. 29:823–833.
- Fin 24. 2015. *Renewables put damper on load shedding*. [Online], Available: <http://www.fin24.com/Economy/Renewables-put-damper-on-load-shedding-20150819> [2015, August 25].
- Foristall, R. 2003. *Heat transfer analysis and modeling of a parabolic trough solar receiver implemented in engineering equation solver*.
- Forsberg, C.W., Peterson, P.F. & Zhao, H. 2007. High-Temperature Liquid-Fluoride-Salt Closed-Brayton-Cycle Solar Power Towers. *Journal of Solar Energy Engineering*. 129(2):141–146.
- Funken, K.-H. 2008. The Jülich Solar Power Tower.

- Hoffmann, J.E. & Van der Merwe, P.C. 2014. Annular solar receiving tube. *SASEC 2014, 27-29 January, Port Elizabeth*.
- Hoffschmidt, B. 2014. *Receivers for Solar Tower Systems*. Font Romeu, France.
- Hongwei Zhu, Ã., Wei, J., Wang, K., Wu, D., Al-Hasan, A.Y., Altermatt, P.P., Kiesewetter, T., Ellmer, K., et al. 2011.
- Howell, J. & Siegel, R. 2011. *Thermal Radiation Heat Transfer*.
- Inglesi-Lotz, R. & Blignaut, J. 2011. *South Africa's electricity consumption: A sectoral decomposition analysis*.
- Kaviany, M. 2012. *Principles of Heat Transfer in Porous Media*. Springer Science & Business Media.
- Kays, W., Crawford, M. & Weigand, B. 2004. *Convective heat and mass transfer*. 4th Editio ed. McGraw-Hill Education.
- Kost, C. 2013. *Levelized cost of electricity renewableenergy technologies*.
- Kröger, D.G. 2011. *The Stellenbosch University Solar Power Thermodynamic Cycle*.
- Mahmoudi, Y. & Karimi, N. 2014. Numerical investigation of heat transfer enhancement in a pipe partially filled with a porous material under local thermal non-equilibrium condition. *International Journal of Heat and Mass Transfer*. 68:161–173.
- Matchdeck. 2015. *Power station refurbishment*. [Online], Available: <https://www.matchdeck.com/article/6601-power-station-refurbishment#/index> [2015, August 25].
- McGregor, J. 2014. *Solar Thermal Foundation Project*.
- Miller, F.J. & Koenigsdorff, R.W. 2000. Thermal Modeling of a Small-Particle Solar Central Receiver. *Journal of Solar Energy Engineering*. 122(1):23.
- Mujeebu, M.A., Abdullah, M.Z., Bakar, M.Z.A., Mohamad, a. a. & Abdullah, M.K. 2009. Applications of porous media combustion technology - A review. *Applied Energy*. 86(9):1365–1375.
- Nield, D. a. & Bejan, A. 2013. *Convection in Porous Media*. Springer.
- NREL. 2015. *Concentrating Solar Power Projects in South Africa*. [Online], Available: [http://www.nrel.gov/csp/solarpaces/by\\_country\\_detail.cfm/country=ZA](http://www.nrel.gov/csp/solarpaces/by_country_detail.cfm/country=ZA) [2015, August 25].
- PYREX. 2013.

- Quero, M., Korzynietz, R., Ebert, M., Jiménez, A.A., del Río, A. & Brioso, J.A. 2014. Solugas – Operation Experience of the First Solar Hybrid Gas Turbine System at MW Scale. *Energy Procedia*. 49:1820–1830.
- Roldán, M.I., Smirnova, O., Fend, T., Casas, J.L. & Zarza, E. 2014. Thermal analysis and design of a volumetric solar absorber depending on the porosity. *Renewable Energy*. 62:116–128.
- Singer, C., Buck, R., Pitz-Paal, R. & Müller-Steinhagen, H. 2010. Assessment of Solar Power Tower Driven Ultrasupercritical Steam Cycles Applying Tubular Central Receivers With Varied Heat Transfer Media. *Journal of Solar Energy Engineering*. 132(4).
- Solarpedia. 2015. *Projects in Green Architecture & Building*. [Online], Available: [http://www.solaripedia.com/13/31/solar\\_one\\_and\\_two\\_\(now\\_defunct\).html](http://www.solaripedia.com/13/31/solar_one_and_two_(now_defunct).html) [2015, June 19].
- SOLGATE Report. 2005. *Solar hybrid gas turbine electric power system*.
- Sonbesie. 2015. *Stellenbosch University solar resource measurement station: Sonbesie metadata*. [Online], Available: <http://weather.sun.ac.za/downloadList.php> [2015, November 02].
- Tian, Y. & Zhao, C.Y. 2013. A review of solar collectors and thermal energy storage in solar thermal applications. *Applied Energy*. 104:538–553.
- Wu, Z., Caliot, C., Flamant, G. & Wang, Z. 2011. Coupled radiation and flow modeling in ceramic foam volumetric solar air receivers. *Solar Energy*. 85(9):2374–2385.

**APPENDIX A. CATALOGUES AND DATA SHEETS**

The following chapter will have all the data sheets available to reproduce the experimental setup, or if further detail is needed with regards to material properties of certain material.

**Table 4: Properties of the glass tube**

<b>Properties</b>	<b>Symbol</b>	<b>Value</b>
Expansion coefficient	$\alpha_{\text{glass}}$	$3.3 \times 10^{-6} \text{ C}^{-1}$
Specific heat constant	$c_{\text{glass}}$	$750 \text{ J/kg}^{\circ}\text{C}$
Thermal conductivity	$k_{\text{glass}}$	$1.14 \text{ W/m}^{\circ}\text{C}$
Density	$\rho_{\text{glass}}$	$2.23 \text{ kg/m}^3$
Poisson's ratio	$\nu_{\text{glass}}$	0.2
Young's modules	$E_{\text{glass}}$	$6.4 \times 10^9 \text{ kg/m}^2$
Refractive index	$n_g$	1.473

Source: (PYREX, 2013)

The table below consist of the equipment used during the testing of the receiver tube. The exact setup of the system can be seen in Chapter 3.

**Table 5: Detail of equipment used**

<b>Type</b>	<b>Manufacturer</b>	<b>Model</b>
Data logger	Agilent	34972A
Thermocouples	N/A	T-type
Pressure regulator	Festo	LRS-QS4-D-I-MINI
Flow meter	Festo	SFAB-600-U-W-Q8-2SV-M12
Transformer	Topward Ltd	6306D
Flux meter	Vatell	TG 1000-0 with AMP-15
Infrared camera	FLIR	E 60

## APPENDIX B. MATLAB CODES

This section will consist of all the MATLAB codes that were written to determine some general properties or to do the numerical analyses.

### B.1 The two-dimensional radiation model

```
%Symmetrical calculations of Project

%% Geometry
%Copper pipe
ri = 7e-3;
ro = 7.5e-3;
Ri = 25e-3;
Ro = 30e-3;

%% Initial variables
phi_start = -90*(2*pi/360);
phi_end = 90*(2*pi/360);
d_phi_i = 15*(2*pi/360);
%d_phi_i = abs((phi_start-phi_end)/itt);
dz = 1.4;
rmax= Ro;
rmin = ro;
dr_i = ((rmax-rmin)/itt);

%% Initial Constants
Ti = 30;
To = 40;           %Outer Boundary value
porous = 0.98;     %Porosity
h_a = 28;         %Convective heat transfer coeff [W/m^2*K]
k_glass = 1.14;
k_air = 0.028;
k_brass = 116;
k_por = porous*k_air + (1-porous)*k_brass;   %Effective thermal
conductivity
nmax = (itt);
mmax = ((phi_end-phi_start)/d_phi_i);
DNI = 933;
CR = 8;
mirr_eff = 0.82;   %mirror efficiency
trans_eff = 0.91; %Transmittance of glass

%% Solar Intensity calculations
Io = DNI*CR*mirr_eff;
Io_transm = Io*trans_eff;
App = Ro*dz;
qrad = Io*App;

% Initial Temperature profile
T = To*ones(mmax,nmax);

%Define area in terms of functions
Am_n = @(r,dr,theta) dz*(r-(dr))*theta; %Area for A(m-1)
Am = @(r,theta) dz*(r)*theta;          %Area for A(m)
```

```

Am_p = @(r,dr,theta) dz*(r+(dr))*theta; %Area for A(m+1)
Am_phi = @(dr) dr*dz;

% Start the code
k = 1;

for k=1:kmax
    phi = phi_start;
    Tk = T; %Store previous temp to determine
    convergence
    for m = 1:mmax
        r = rmax; %Start at the outer radius again
        % The angle is only half for the area at the outer iterations
        if m==1 || m==mmax
            d_phi = d_phi_i/2 ;
        else
            d_phi = d_phi_i;
        end
        for n = 1:nmax
            %The radius element is only half for the outer iterations
            if n == 1 || n==nmax
                dr = dr_i/2 ;
            else
                dr = dr_i;
            end

            x(m,n) = r*cos(phi);
            y(m,n) = r*sin(phi);

            if x(m,n)>ro || y(m,n)<0 %Include the shadow of the
copper pipe

                if n==1 %Assume parrallel rays coming in
                    zeta_i = max((abs(-(y(m,n)))-sqrt(Ri^2-(abs(x(m,n))^2))),0);
                    zeta_o = (zeta_i+dr/2);
                else if n>1 && n<nmax
                    zeta_i = max((abs(-(y(m,n)))-sqrt(Ri^2-(abs(x(m,n))^2)))-
(dr/2),0);
                    zeta_o = (zeta_i+dr);
                else
                    zeta_i = max((abs(-(y(m,n)))-sqrt(Ri^2-
(abs(x(m,n))^2)))- (dr/2),0);
                    zeta_o = (zeta_i+dr/2);
                end
            end
        else
            zeta_i = inf;
            zeta_o = inf;
        end

        %Use different thermal conductivity values
        if r>Ri
            k_eq = k_glass;
            edot = @(SS,A) (Io*A);
        else
            k_eq = k_por;
            edot = @(SS,A) (Io_transm*exp(-kappa*(SS))*A);
        end
    end
end

```

```

%Constants that will be used regularly.
Cw = k_eq*Am_phi(dr)/dr;
Cs = k_eq*Am_p(r,dr,d_phi)/dr;
Cs_o = h_a*Am(r,d_phi);
Ce = Cw;
Cn = k_eq*Am_n(r,dr,d_phi)/dr;

if m==1
    Cw = 0;
    if n==1
        %Include convection in outer cylinder
        Cs = h_a*Am(r,d_phi);
        Tnew(m,n) =
(1/(Cw+Cs_o+Ce+Cn))*(Cs_o*To+Ce*T(m+1,n)+Cn*T(m,n+1)+edot(zeta_i,Am_p(
r,dr,d_phi))-edot(zeta_o,Am_n(r,dr,d_phi)));
        Qnet(m,n) = Cs_o*(To-Tnew(m,n))+Ce*(T(m+1,n)-
Tnew(m,n))+Cn*(T(m,n+1)-Tnew(m,n))+edot(zeta_i,Am_p(r,dr,d_phi))-
edot(zeta_o,Am_n(r,dr,d_phi));
        else if n>1 && n<nmax
            Tnew(m,n) = (1/(Cw+Cs+Ce+Cn))*(Cs*T(m,n-
1)+Ce*T(m+1,n)+Cn*T(m,n+1)+edot(zeta_i,Am_p(r,dr,d_phi))-
edot(zeta_o,Am_n(r,dr,d_phi)));
            Qnet(m,n) = -Cs*(Tnew(m,n)-T(m,n-
1))+Ce*(T(m+1,n)-Tnew(m,n))+Cn*(T(m,n+1)-
Tnew(m,n))+edot(zeta_i,Am_p(r,dr,d_phi))-
edot(zeta_o,Am_n(r,dr,d_phi));
        else
            Tnew(m,n) = (1/(Cw+Cs+Ce+Cn))*(Cs*T(m,n-
1)+Ce*T(m+1,n)+Cn*Ti+edot(zeta_i,Am_p(r,dr,d_phi))-
edot(zeta_o,Am_n(r,dr,d_phi)));
            Qnet(m,n) = -Cs*(Tnew(m,n)-T(m,n-
1))+Ce*(T(m+1,n)-Tnew(m,n))+Cn*(Ti-
Tnew(m,n))+edot(zeta_i,Am_p(r,dr,d_phi))-
edot(zeta_o,Am_n(r,dr,d_phi));
        end
    end

else if m>1 && m <mmax
    if n==1
        %Include convection in outer cylinder
        Cs = h_a*Am(r,d_phi);
        Tnew(m,n) = (1/(Cw+Cs_o+Ce+Cn))*(Cw*T(m-
1,n)+Cs_o*To+Ce*T(m+1,n)+Cn*T(m,n+1)+edot(zeta_i,Am_p(r,dr,d_phi))-
edot(zeta_o,Am_n(r,dr,d_phi)));
        Qnet(m,n) = -Cw*(Tnew(m,n)-T(m-1,n))+Cs_o*(To-
Tnew(m,n))+Ce*(T(m+1,n)-Tnew(m,n))+Cn*(T(m,n+1)-
Tnew(m,n))+edot(zeta_i,Am_p(r,dr,d_phi))-
edot(zeta_o,Am_n(r,dr,d_phi));
        else if n>1 && n<nmax
            Tnew(m,n) = (1/(Cw+Cs+Ce+Cn))*(Cw*T(m-
1,n)+Cs*T(m,n-
1)+Ce*T(m+1,n)+Cn*T(m,n+1)+edot(zeta_i,Am_p(r,dr,d_phi))-
edot(zeta_o,Am_n(r,dr,d_phi)));
            Qnet(m,n) = -Cw*(Tnew(m,n)-T(m-1,n))-
Cs*(Tnew(m,n)-T(m,n-1))+Ce*(T(m+1,n)-Tnew(m,n))+Cn*(T(m,n+1)-
Tnew(m,n))+edot(zeta_i,Am_p(r,dr,d_phi))-
edot(zeta_o,Am_n(r,dr,d_phi));
        else

```

```

                                Tnew(m,n) = (1/(Cw+Cs+Ce+Cn))* (Cw*T(m-
1,n)+Cs*T(m,n-1)+Ce*T(m+1,n)+Cn*Ti+edot(zeta_i,Am_p(r,dr,d_phi))-
edot(zeta_o,Am_n(r,dr,d_phi)));
                                Qnet(m,n) = -Cw*(Tnew(m,n)-T(m-1,n))-
Cs*(Tnew(m,n)-T(m,n-1))+Ce*(T(m+1,n)-Tnew(m,n))+Cn*(Ti-
Tnew(m,n))+edot(zeta_i,Am_p(r,dr,d_phi))-
edot(zeta_o,Am_n(r,dr,d_phi));
                                end
                                end

                                else      %if m==mmax --> last control volume (on
copper pipe)
                                Ce = 0;
                                if n==1
                                %Include convection in outer cylinder
                                Cs = h_a*Am(r,d_phi);
                                Tnew(m,n) = (1/(Cw+Cs_o+Ce+Cn))* (Cw*T(m-
1,n)+Cs_o*To+Cn*T(m,n+1)+edot(zeta_i,Am_p(r,dr,d_phi))-
edot(zeta_o,Am_n(r,dr,d_phi)));
                                Qnet(m,n) = -Cw*(Tnew(m,n)-T(m-1,n))+Cs_o*(To-
Tnew(m,n))+Cn*(T(m,n+1)-Tnew(m,n))+edot(zeta_i,Am_p(r,dr,d_phi))-
edot(zeta_o,Am_n(r,dr,d_phi));
                                else if n>1 && n<nmax
                                Tnew(m,n) = (1/(Cw+Cs+Ce+Cn))* (Cw*T(m-
1,n)+Cs*T(m,n-1)+Cn*T(m,n+1)+edot(zeta_i,Am_p(r,dr,d_phi))-
edot(zeta_o,Am_n(r,dr,d_phi)));
                                Qnet(m,n) = -Cw*(Tnew(m,n)-T(m-1,n))-
Cs*(Tnew(m,n)-T(m,n-1))+Cn*(T(m,n+1)-
Tnew(m,n))+edot(zeta_i,Am_p(r,dr,d_phi))-
edot(zeta_o,Am_n(r,dr,d_phi));
                                else
                                Tnew(m,n) = (1/(Cw+Cs+Ce+Cn))* (Cw*T(m-
1,n)+Cs*T(m,n-1)+Cn*Ti+edot(zeta_i,Am_p(r,dr,d_phi))-
edot(zeta_o,Am_n(r,dr,d_phi)));
                                Qnet(m,n) = -Cw*(Tnew(m,n)-T(m-1,n))-
Cs*(Tnew(m,n)-T(m,n-1))+Cn*(Ti-
Tnew(m,n))+edot(zeta_i,Am_p(r,dr,d_phi))-
edot(zeta_o,Am_n(r,dr,d_phi));
                                end
                                end
                                end
                                end

                                if n==nmax
                                T(m,n) = Tnew(m,n);
                                break
                                else
                                %update new value
                                T(m,n) = Tnew(m,n);
                                n = n+1;
                                r = r-dr_i;
                                storer(m,n)=r;
                                end
                                end

%Update new values
if m == mmax
    T(m,n) = Tnew(m,n);
    break
else

```

```

    T(m,n) = Tnew(m,n);
    m = m+1;
    phi = phi + d_phi;
end
end

%Check for convergence
for kk=1:size(T,1)
    for ll=1:size(T,2)
err(kk,ll) = abs(1-(Tnew(kk,ll)/(Tk(kk,ll))));
    end
end
max_error(k) = max(max(err));
if max_error(k) <tol
    break
else
    T = Tnew+(alpha*(max_error(k)^betha)*Tnew);
    k = k+1;
end
end

```

## B.2 Deflection analyses of structure

```

%Calculate the deflection in the beam supporting the mirrors

l = 0.96; %length of beam considered

%demensions of tubing
thickness = 2e-3;
tube.out = 31.7e-3;
tube.in = tube.out - 2*thickness;

I = (tube.out^4-tube.in^4)/12; %Moment of inertia
E = 200e9; %Young's Modules

L_tube = 7.7; %length of total tubing
spes_mass_tube = 1.894 %Massa per length

mass.tube = L_tube*spes_mass_tube; %total mass of tube
mass.mirr = 20.64; %mass of mirrors
mass.plate = 20; %Mass of support plate of mirrors
mass.tot = mass.tube+mass.mirr+mass.plate

%force on support
P = mass.tot*9.81;
w = P/l

%Deflection and anles at end points
def = (5*w*l^3)/(384*E*I)
theta = (w*l^3)/(24*E*I)
theta_deg = theta*(180/pi)

```

## APPENDIX C. CALIBRATION OF INSTRUMENTS

This section will consist of the techniques and data used to calibrate the instruments, which include the thermocouples, pressure regulators, flow meters and flux measurements.

### C.1 Calibration of the flow meter and pressure regulator

The basis calibration of the flow meter and the pressure regulator will be done by using a bell mouth and orifice plate, as shown in Figure 49. The bell mouth and the orifice plate have the following dimensions:

**Table 6: Dimensions of bell mouth and orifice plate**

Bell Mouth	$D_1 = 32\text{mm}$	$d_2 = 3\text{mm}$
Orifice Plate	$D_1 = 12.5\text{mm}$	$d_2 = 4\text{mm}$

The following steps were used to calibrate the two meters:

1. Open  $V_o$
2. Open  $V_2$  and open  $V_1$  measure  $h_{a1} = h_a$  and  $h_o$
3. Close  $V_1$  and open  $V_2$  measure  $h_{a2} = h_a$  and  $h_o$
4. Measure atmospheric pressure, the temperature of the air and the water.

The flow meter will be calibrated using the orifice plate, with the following general formulation done by Çengel and Cimbala (2009):

$$\dot{V} = A_o C_d \sqrt{\left( \frac{2(P_1 - P_2)}{\rho \left(1 - \left(\frac{d}{D}\right)^4\right)} \right)} \quad \text{C.1}$$

where:

$$A_o = \frac{\pi d^2}{4} \quad \text{C.2}$$

$$C_d = 0.5959 + 0.0312 \left(\frac{d}{D}\right)^4 - 0.184 \left(\frac{d}{D}\right)^8 + \frac{91.71 \left(\frac{d}{D}\right)^{2.5}}{Re^{0.75}} \quad \text{C.3}$$

The pressure regulator will be calibrated by using the bell mouth. The absolute temperatures will be subtracted from each other to get a pressure drop. The readings  $h_{a1}$  and  $h_{a2}$  will be used. The pressure drop can be converted to Pascal's by using Newton's second Law:

$$P_{abs} = \rho_{mercury} g h_a \quad C.4$$

The experimental setup can be seen in Figure 49. The pressure regulator and the flow meter are installed in series just before the inlet of the air at the bell mouth. The valve  $V_o$  is a safety valve to avoid and injuries.

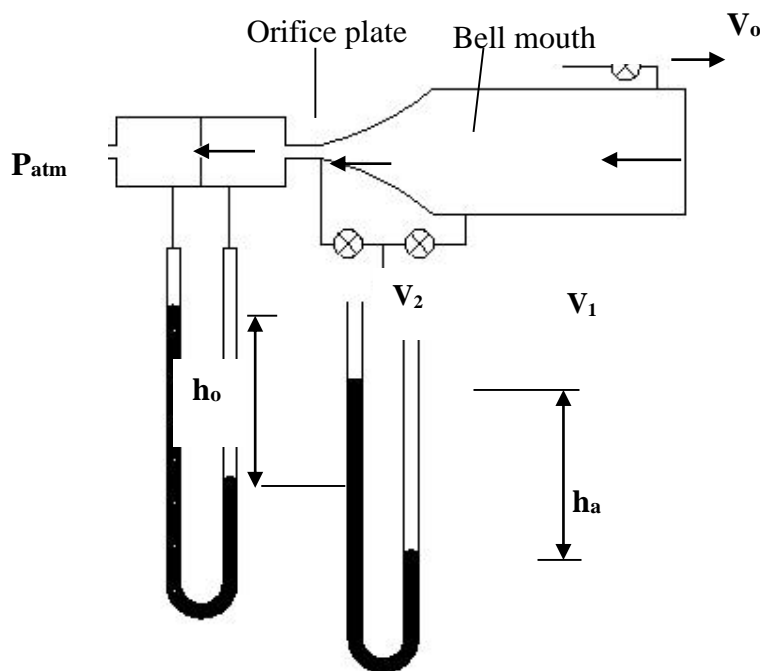


**Figure 49: Experimental setup**

The calibration curves of the flow meter and the pressure regulator can be seen in Figure 50 and Figure 51 respectively. These two graphs show that the measuring devices are well within the error limits. The errors are small enough to suggest that they could be due to a large variety of effects. Since these errors are small enough, the instruments will be assumed to be perfect and that no variation will have to be made to the measured data.

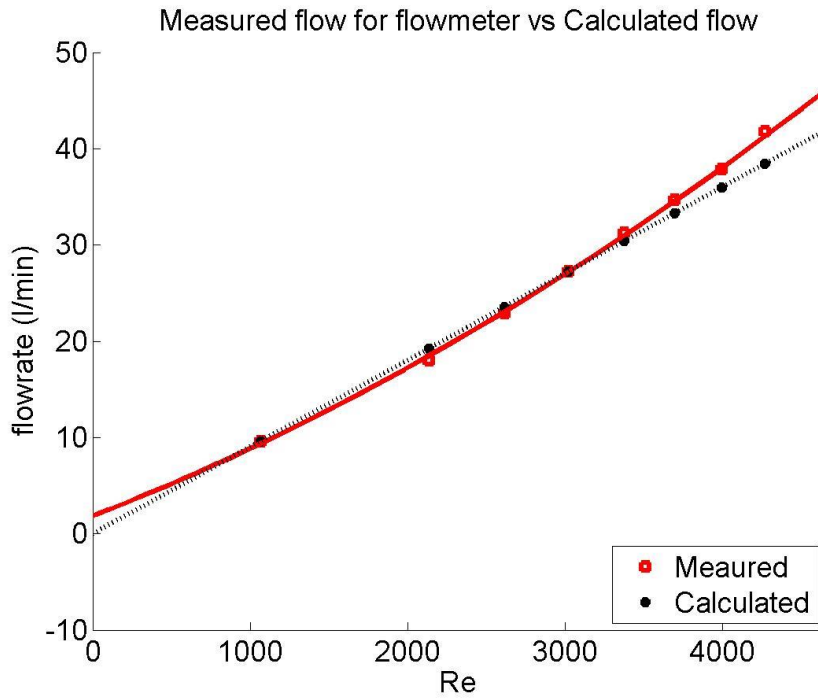


Figure 50: Calibration of the flow meter

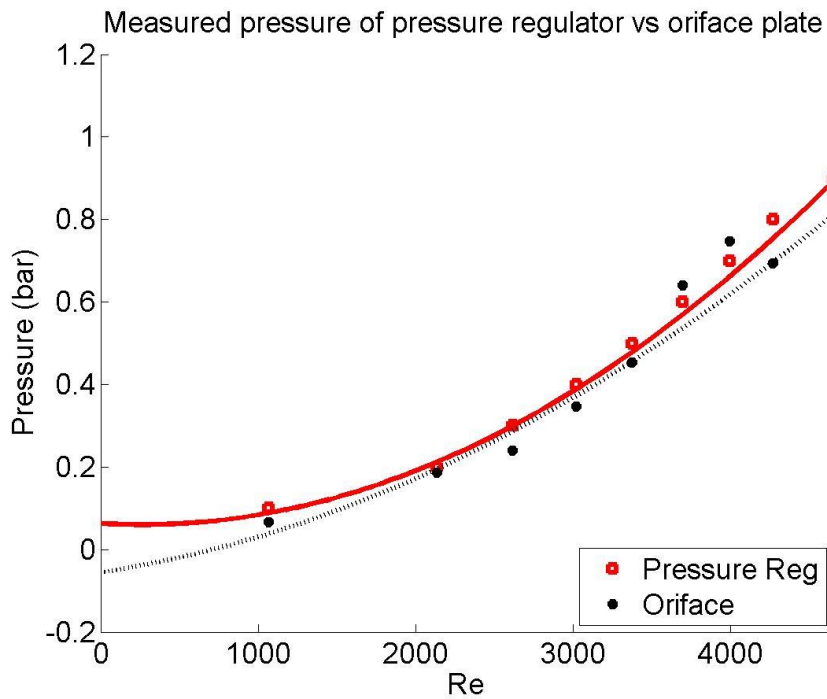


Figure 51: Calibration of the pressure regulator

## C.2 Calibration of flux sensor

As previously discussed, it was not able to conduct synchronized concentrated flux measurements during the testing. The receiver tube was thus removed from the frame and the flux sensor was placed where the receiver should be to determine the concentrated flux at that point for a specific flux. It can be seen that the flux meter was first calibrated to the DNI from the sun for the first 40 readings, and was then moved to the concentrated part.

The average of the concentrated flux were taken over four different readings. The average flux was measured to be  $6524 \text{ W/m}^2$  and the average DNI value from Sonbesie was  $927 \text{ W/m}^2$ . The efficiency of the mirrors was then calculated to be 88 %, compared to the manufacturer specification of 83 %. This is an error of five per cent, which is acceptable for the amount of uncertainties that is present. This calibration test in Figure 52 was done on the 2<sup>nd</sup> of March 2015 between 14:15 and 14:55 in the afternoon.

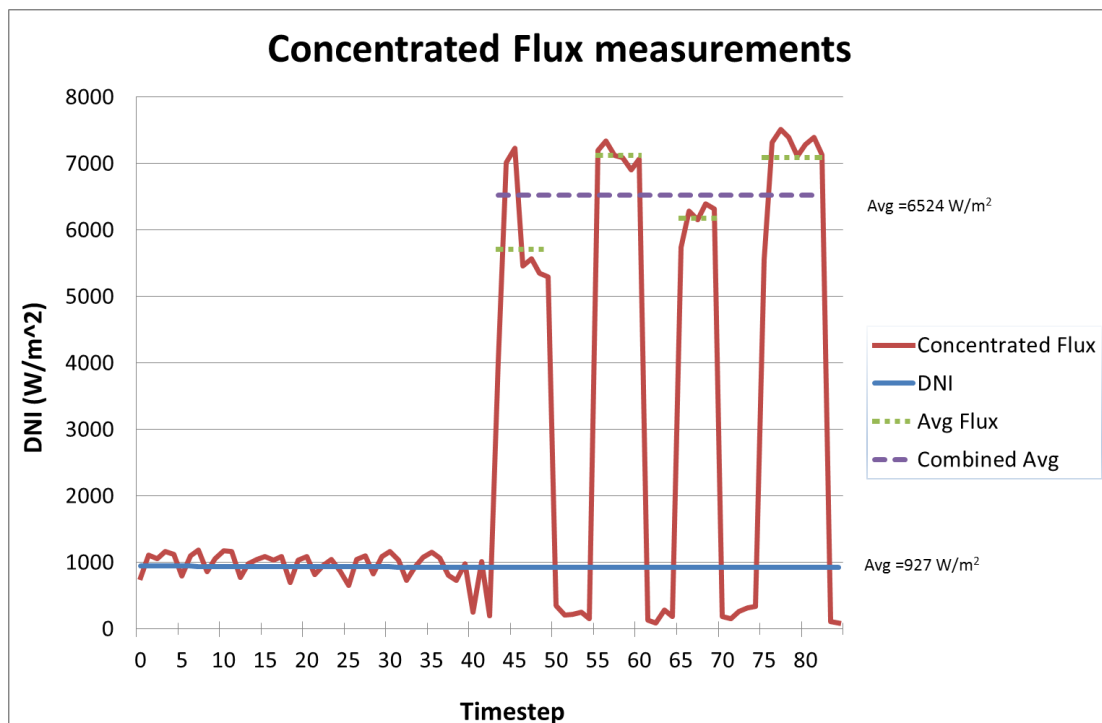
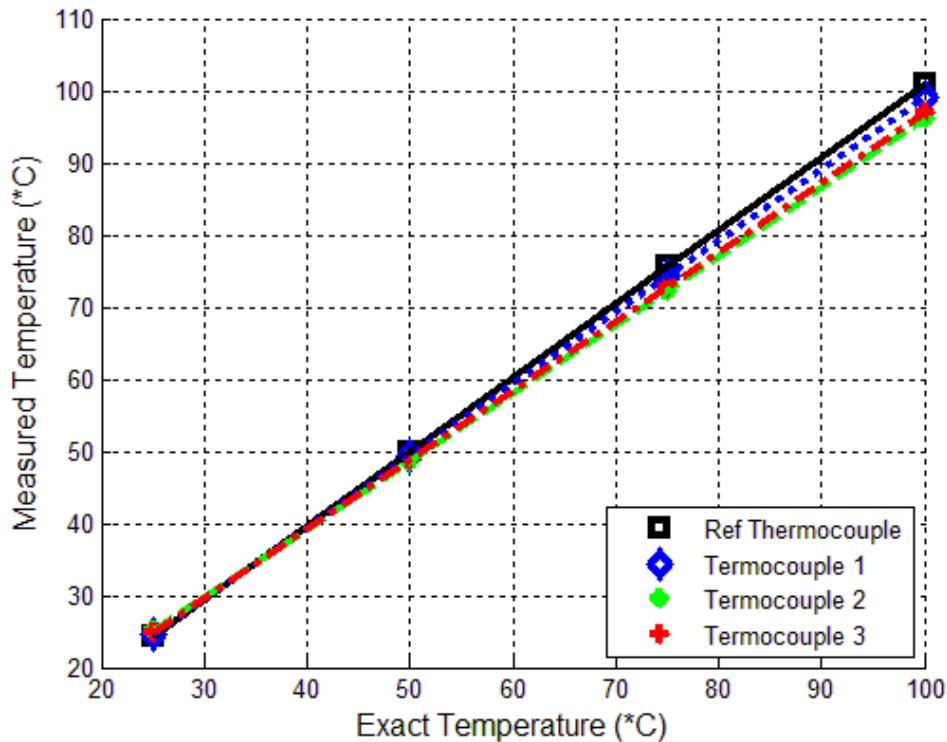


Figure 52: Calibration of the flux at outer surface

### C.3 Thermocouple calibration

The thermocouples were calibrated by a Fluke calibration machine. There were four reference points used: 25 °C, 50 °C, 75 °C, and 100 °C. The temperature of the air will never exceed these limits. The temperature measurements at steady state were compared to the reference thermocouple, which is calibrated yearly.



**Figure 53: Calibration graph of some thermocouples**

Each thermocouple is fitted with a linear equation which is temperature dependant. This equation is stored and used for every data point measured during testing to determine the error in measurement. An example of this can be seen below:

$$T_{exact} = c_1 T_{mes} + c_2 \quad C.5$$

For Thermocouple 1, the value of  $c_1 = 0.07986$  and  $c_2 = -2.72$  which mean that for a measured temperature of 55 °C, the difference 1.7 °C, which mean the actual temperature is 56.7 °C.

Figure 53 shows the temperature differences compared to the reference thermocouple for some of the thermocouples. Not all the thermocouples are plotted, since it will be too confusing and not clear, but these temperature differences of all the thermocouples can, however, be seen in Table 7 below.

**Table 7: Temperature difference of all the thermocouples**

	<i>Temperature difference @</i>			
	25 °C	50 °C	75 °C	100 °C
<b>Thermocouple 1</b>	-0.7	1.3	3.3	5.3
<b>Thermocouple 2</b>	-0.6	1.6	3.8	6.0
<b>Thermocouple 3</b>	-0.7	0.9	2.6	4.3
<b>Thermocouple 4</b>	-0.7	1.5	3.7	5.9
<b>Thermocouple 5</b>	-0.6	1.8	4.2	6.6
<b>Thermocouple 6</b>	-0.2	0.5	1.3	2.1
<b>Thermocouple 7</b>	-0.5	1.3	3.1	5.0
<b>Thermocouple 8</b>	-0.5	1.3	3.1	4.8
<b>Thermocouple 9</b>	-0.2	0.6	1.5	2.3
<b>Thermocouple 10</b>	-0.3	1.2	2.6	4.0
<b>Thermocouple 11</b>	-0.5	1.4	3.2	5.0
<b>Thermocouple 12</b>	-0.4	1.4	3.2	5.0
<b>Thermocouple 13</b>	-0.4	1.6	3.6	5.6
<b>Thermocouple 14</b>	-0.5	1.5	3.4	5.4

## APPENDIX D. EXPENSES OF PROJECT

There are a lot of different costs involved in product development, some of which is not accurately measurable, but can be estimated. These include the cost of handling and using of equipment during testing and the exact time of different aspects of the project.

**Table 8: The cost for each activity**

Activity	Engineering time	
	hr	R
Literature Study	200	R 70 000.00
Identify equipment needed	16	R 5 600.00
Setup Design variables	16	R 5 600.00
Formulate Concepts	80	R 28 000.00
Optimize best concept	80	R 28 000.00
Design Review	16	R 5 600.00
Design Experimental Model	160	R 56 000.00
Setup of Experimental Model	160	R 56 000.00
Tests of Experimental Model	120	R 42 000.00
Create Numerical Model	320	R 112 000.00
Create CFD Model	120	R 42 000.00
Annalise Results	240	R 84 000.00
Report Writing	320	R 112 000.00
	<b>1848</b>	<b>R 646 800.00</b>

The expenses associated with consumables used for the development of the receiver tube can be seen in Table 10, with the general expenses being all the small items, like glue, rubber straps etc. Although only one quarts tube was used, a back-up tube was also ordered in case of failure.

**Table 9: Expenses for construction of rig**

Product	Amount	Price per unit	Total
Square tubing 31.7 x 2 x 0.6	3	R 159.23	R 477.69
Silver mirrors 1400 x 100 x 3	8	R 342.00	R 2 736.00
Mirror back plates	8	R 141.21	R 1 129.68
Festo pressure regulator	1	R 2 808.00	R 2 808.00
Copper pipe	1	R 190.00	R 190.00
Plastic Spacers	2	R 145.00	R 290.00
Quarts tube	2	R 1 227.00	R 2 454.00
General Expenses	1	R 505.00	R 505.00
Fasteners	55	R 3.50	R 192.50
			R 10 782.87

**Table 10: Expense of equipment used (depreciation)**

Equipment	Fraction	Product Cost	Total
Flowmeter	0.015	R 5 000.00	R 76.92
Transformer	0.015	R 2 000.00	R 30.77
Data Logger	0.015	R 30 000.00	R 461.54
Flux Sensor	0.004	R 20 000.00	R 76.92
Computer	0.400	R 7 000.00	R 2 800.00
			R 3 446.15

Borrowed equipment were priced in according to a depreciation value. The fraction value that is used to calculate the depreciation value, differs for the different equipment. A lifespan, in years, was estimated for each one, times the fraction of the time it was used during the year. Each equipment were estimated at a certain value, which was timed by the depreciation factor to get the estimate cost of using the equipment. The lifespan for a computer was estimated to be 5 years, whereas for a flow meter of data logger, it was estimated at 10 years.

The total project cost, excluding the rent of any buildings or resources, can be seen in Table 11. The total project cost adds up to an amount of R 661 029, which is relatively high for such a small project. It is clear that the biggest expense in a project is human resources.

**Table 11: Total project cost**

Type	Cost
Activity cost	R 646 800.00
Equipment cost	R 3 446.15
Expenses	R 10 782.87
	R 661 029.02

**APPENDIX E. DIMENSIONED DRAWING**

